Modeling, Manufacturing, and Experimental Validation of an Electric Machine for Aircraft Propulsion

by

Henry Andersen

B.S. Electrical Engineering and Computer Science, Massachusetts Institute of Technology (2022)

Submitted to the Department of Electrical Engineering and Computer Science
in partial fulfillment of the requirements for the degree of

MASTER OF ENGINEERING IN ELECTRICAL ENGINEERING AND COMPUTER SCIENCE

at the

MASSACHUSETTS INSTITUTE OF TECHNOLOGY

February 2024

Authored by:	Henry Andersen Department of Electrical Engineering and Computer Science February 4, 2024
Certified by:	Jeffrey H. Lang Vitesse Professor of Electrical Engineering, Thesis Supervisor
Accepted by:	Katrina LaCurts Chair, Master of Engineering Thesis Committee

Modeling, Manufacturing, and Experimental Validation of an Electric Machine for Aircraft Propulsion

by

Henry Andersen

Submitted to the Department of Electrical Engineering and Computer Science
on February 4, 2024 in partial fulfillment of the requirements for the degree of

MASTER OF ENGINEERING IN ELECTRICAL ENGINEERING AND COMPUTER SCIENCE

ABSTRACT

The work presented in this thesis is part of an effort at MIT to develop a 1-MW electric machine which achieves the specific power necessary for hybrid-electric aviation: 13 kW/kg [1]. The models for torque and core loss used in the design of the 1-MW machine are revised and expanded based on experimental results obtained from a partially-manufactured prototype to guide the design of future high specific-power electric machinery.

To calculate the torque produced by the machine, the air-gap field created by a segmented Halbach array rotor is derived from Maxwell's Equations. The closed-form solution for the air-gap field matches Finite Element Analysis (FEA) to within 1% and experimental data from the manufactured prototype to within the tolerance of the experiment. A method for modeling a slotted stator as a smooth cylinder with a surface current is applied to the stator of the 1-MW machine, and the average torque and torque ripple are calculated using the Lorentz-Kelvin force density. The analytical torque calculation computes 100,000 times faster than 2D FEA (0.56 ms vs. 44 s), and matches FEA to within 1.2%, making it ideal for initial machine design.

An experimental procedure is developed to measure the core loss and B-H curve of an iron lamination stack. This procedure is applied to various toroid samples and a stack of slotted stator laminations. A conventional lamination bonding process is found to raise core loss by 20% for 0.1-mm iron-cobalt laminations. An alternative stator-core manufacturing process, which results in no impact on core loss, is identified and experimentally verified. Based on the measured core loss of a stack of stator laminations, the 1-MW prototype is expected to remain within the thermal limits imposed by the winding insulation.

Thesis supervisor: Jeffrey H. Lang
Title: Vitesse Professor of Electrical Engineering

Acknowledgments

I would like to thank Lana Salve for her unconditional love and support over the last six years. She gives me a reason to smile and laugh every single day. I never would have made it this far without her.

Professor Jeffrey Lang has served as my role model at MIT. I am constantly inspired by his patience, commitment to helping students, and vast technical knowledge. He helped me to resolve the issues I faced with every single experiment and model in this thesis.

Dr. Aidan Dowdle mentored me over the first six months that I worked on the 1-MW project. His patience and kindness as I came up to speed were more than I could have asked for. The work in this thesis is based on the incredible effort that he put into project throughout his time as Ph.D. student.

Mr. Marc Amato has taught me so much about engineering and life in general. His effort and guidance on the 1-MW project has been the key to our success so far.

Professor Zoltan Spakovszky has provided me with the opportunity to work on this incredibly exciting project while travelling around the world. His insight and guidance in our weekly meetings have shaped the work in this thesis and helped me to improve my technical communication skills.

The 1-MW project is a true team effort, and it would not be possible without the hard work of every single team member: Dr. David Gonzales Cuadrado, Dr. Yuankang Chen, Dr. Mohammad Qasim, David Otten, Brian Robinson, Aneesh Jois, Charlotte Gump, Professor Edward Greitzer, Professor James Kirtley, Professor David Perreault, Professor Zachary

Cordero, Pam Fradkin and Jennifer Leith. It has been a pleasure getting to know every single one of you.

My sister Lila has always been there for me through thick and thin, ready to make me laugh. I am extremely grateful for all of the love and support from my Mom, Dad, Erik, Pete, Jolene, and the rest of my extended family. Thank you all.

I would like to thank all of my friends at MIT: Joachim, Sofia, Zhibo, Lasse, Aneesh, Hiro, Maranda, Ben and the rest of the students at the GTL, and my friends in Berkeley: Gaurav, Roi, Royce, Zack, and Kian for all of the great times over the past couple of years.

Tommy Krause started my passion for electric motors two years ago with his help on my 6.131 final project. Since then, he has been a patient mentor, always ready for a discussion on electric machinery.

Funding for this work was provided by Mitsubishi Heavy Industry, Ltd. It was an honor to collaborate with their skilled team of engineers, including Sasaki-san, Iida-san, Ezumi-san, and Mifune-san.

Contents

List of Figures

List of Tables

Chapter 1

Introduction

1.1 Background

Inspired by the success of the electrification of the automotive industry, the commercial airline industry has identified electrified aircraft as the future of aviation. The largest motivation behind the transition to electric aviation is to reduce the 1 billion tons of CO_2 produced annually by the aviation industry, a number that will compound as the commercial air travel industry continues to grow [2]. Other benefits to electric aviation include increased reliability, less engine noise, and greater freedom in aircraft design.

Although batteries currently lack the energy density required to power the commercial airliners responsible for 95% of airplane CO_2 emissions, partially-electrified aircraft designs, such as the NASA STARC-ABL, offer promising improvements in fuel efficiency [1], [3]. In order to realize large-scale electric aircraft, megawatt-class electric machinery with a specific power exceeding 13 kW/kg is necessary [1].

The work presented in this thesis is part of collaboration between the MIT Gas Turbine Laboratory, the MIT Laboratory for Electromagnetic and Electronic Systems, and Innova-Logic LLC to develop, manufacture, and demonstrate a 1-MW electric machine which is expected to achieve a specific power of 17 kW/kg.

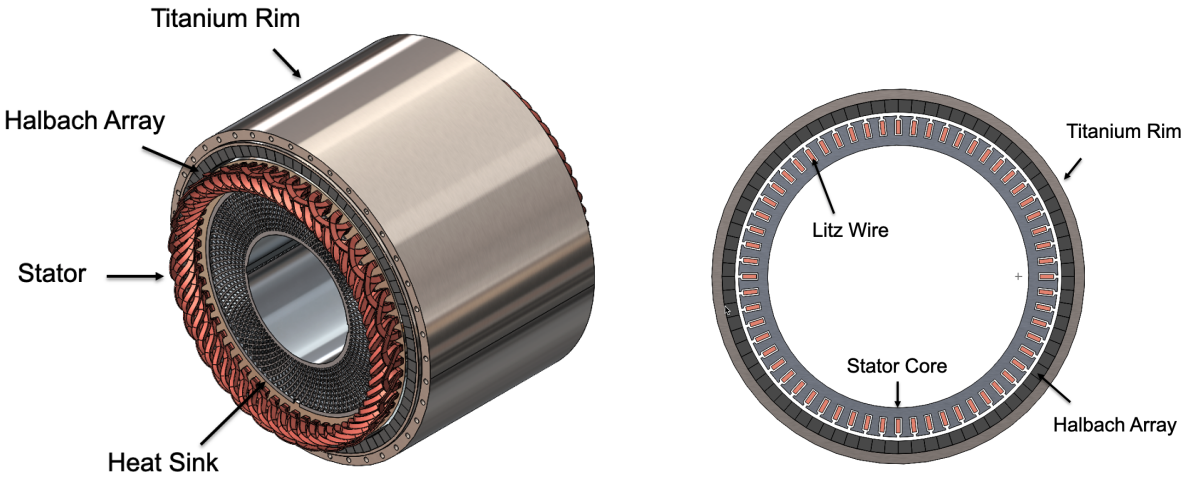

(a) Isometric view

(b) Front view, without heat sink

Figure 1.1: High specific-power electric machine for aircraft propulsion.

Dr. Aidan Dowdle completed the electromagnetic design of the electric machine, from an initial integrated prime mover concept to the manufactured demonstrator, shown in Figure 1.1. The full details of the electromagnetic design process of the 1-MW demonstrator are given in Dowdle (2022) [4]. In this thesis, the models used by Dowdle (2022) for torque and stator core loss are revised and expanded based on experimental data collected from a partially-manufactured prototype of the machine in Figure 1.1. The manufactured prototype is referred to as the "1-MW demonstrator" throughout this thesis.

Dr. Yuankang Chen completed the thermal and mechanical design of the 1-MW demonstrator, as described in Chen (2023) [5]. Dr. Mohammad Qasim and Mr. David Otten designed the power electronic drive for the 1-MW demonstrator, as described in Qasim (2024) [6]. Dr. David Gonzales Cuadrado designed the superstructure and laboratory setup used for testing the 1-MW demonstrator. Full power testing of the 1-MW demonstrator is planned for later in 2024.

Metric		Value	Units
Power		1	MW
Specific Power		17	kW/kg
Speed		12,500	RPM
Shear stress		5.3	PSI
Efficiency		97.3 %	-
Slot current density (peak)		13.3	A/mm^2
Number of pole pairs / slots		10 / 60	-
Size	Stack length	198	mm
	Outer diameter	300	mm
	Air gap	3	mm
Material	Stator core	Vacodur 49, 0.1 mm	Fe-Co-V
	Winding	Litz Type 8	Cu
	Permanent magnet	Recoma® 35E	Sm-Co
	Retaining sleeve	Titanium	Ti

Table 1.1: Electric machine design specifications.

1.2 Overview of Electric Machine Design

A brief overview of the electromagnetic design of the 1-MW demonstrator is given in this section to provide context for the work completed in this thesis.

A trade-space analysis of electric machine architectures found that the outer-rotor, radial-flux, surface-mounted permanent-magnet synchronous machine (PMSM) achieves the optimal combination of power density and thermal feasibility for aircraft propulsion [4], [5]. The outer-rotor architecture and air-cooled thermal-management system enable the machine to be directly integrated inside a turbomachine as a generator. An integrated-prime-mover concept using this electric machine is proposed in [4]. Fundamental design details such as geometry, speed, torque, and pole count were co-optimized considering the structural feasibility, weight, and efficiency the electric machine, the thermal management system, and the power electronics drive [4]–[6].

A structural view of the electric machine is shown in Figure 1.1. The key metrics of the design are presented in Table 1.1. The Halbach-array rotor eliminates the need for rotor back iron. Instead, a light-weight titanium rim is used to retain the permanent magnets.

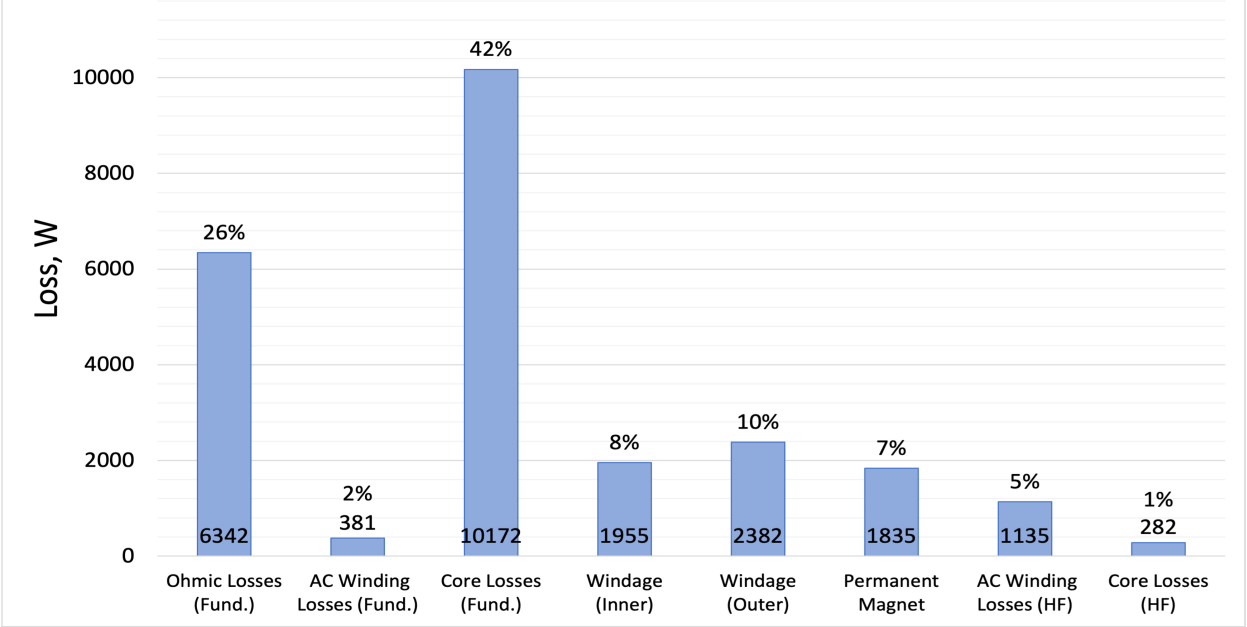

Figure 1.2: Breakdown of electric machine loss.

Component	**Mass [kg]**
Stator Core	19.7
Windings	6.1
Magnets	14.6
Rim	10.6
Heat sink	6.4
Total	**57.4**

Table 1.2: Breakdown of electric machine mass.

Within the Halbach array, the use of four directions of magnetization per pole decreases the harmonic distortion of the air-gap flux density and reduces torque ripple to 1% of the average torque, as discussed in Chapter 2. 0.1-mm iron-cobalt stator laminations mitigate core loss and Litz wire mitigates Ohmic loss at the high operational electrical frequency, 2083 Hz. A modular, single-phase winding pattern improves reliability and enables single-phase inverter drives. A 3D-printed aluminum heat sink enables air-cooling at full power.

Figure 1.2 shows the predicted loss of the electric machine. Stator core loss is estimated through FEA using experimentally-measured data, collected as discussed in Chapter 3. Permanent-magnet loss is calculated through FEA using material data provided by the magnet vendor. The Ohmic and windage losses are calculated with models described

in Dowdle (2022) and Chen (2023) respectively [4], [5]. The specific power of the electric machine is calculated using the mass in Table 1.2. The superstructure and bearing system masses are not included in the specific power calculation because they would change depending on the application of the machine, and therefore they are not optimized for specific power.

1.3 Related Work

There are many ongoing efforts to build high-specific-power, megawatt-class electric machinery for aircraft propulsion, ranging from projects at large companies such as Airbus, GE, and Rolls-Royce to projects at smaller companies such as H3x, Hinetics, and Nidec Aerospace to projects at universities such as University of Illinous, Urbana-Champaign (UIUC), University of Wisconsin, Madison (UW), and MIT. Because only limited information has been published about the machines under development from the companies listed above, this section focuses on the ongoing projects at the other two universities, UIUC and UW.

At UIUC, Lee et al. (2023) have manufactured a 300-kW, outer-rotor, Halbach array, slotless stator prototype of the machine shown in Figure 1.3a. This machine is air-cooled by a fan embedded in the rotor and a heat sink inside of the stator, and is designed to operate at 3,600 rpm. The authors plan to use the results from testing this prototype to manufacture a scaled, higher-speed, 833 kW version of the machine in shown in Figure 1.3a. The UIUC machine and the MIT machine are similar in many regards, for instance both have outer-rotor Halbach arrays and air-cooling. However, the largest difference between the machines is that the UIUC machine has a slotless stator with ceramic-potted windings that is believed to increase the specific power of the machine, whereas the MIT machine employs a more conventional slotted stator while still achieving the specific power target of 13 kW/kg to enable hybrid-electric aviation [1].

At UW, Swanke et al. (2021) have manufactured a 200 kW, inner-rotor, non-Halbach

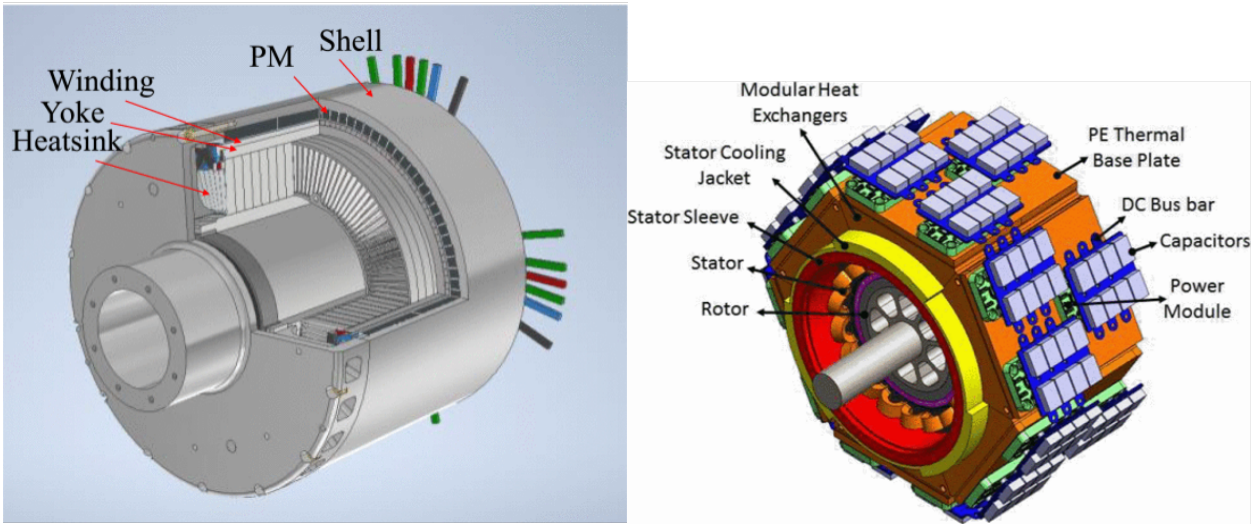

(a) Figure 1 from Lee et al. (2023) [7]

(b) Figure 1 from Swanke et al. (2021) [8]

Figure 1.3: Other electric machines for aircraft propulsion under development at (a) UIUC (b) UW.

array, slotted stator prototype of the machine shown in Figure 1.3b. This machine is liquid-cooled with a stator cooling jacket, and is designed to operate at 20,000 rpm. The authors plan to use the results from testing this prototype to manufacture a scaled, 1-MW version of the machine in shown in Figure 1.3b. The largest differences between the MIT machine and the UW machine are that the MIT machine is air-cooled and has an external rotor to enable integration inside of a turbomachine as a generator, whereas the UW machine is liquid-cooled and has an interior rotor. The more conventional interior rotor of the UW machine enables higher rotational speeds because the rotor is supported with bearings on both sides of the machine. To use the UW machine as turbo-electric generator, an additional shaft connecting the electric machine and the gas turbine engine and an additional liquid-cooling system would likely be needed, increasing the overall weight of the system. This suggests that the UW machine is not intended for use as a turbo-electric generator.

1.4 Contributions

The goal of this thesis is to revise and expand the models for torque and stator core loss used by Dowdle (2022) to design the 1-MW machine in Figure 1.1, based on experimental data collected from a partially-manufactured prototype of the machine.

In Chapter 2, the air-gap magnetic field produced by a cylindrical, segmented Halbach-array rotor is derived from Maxwell's Equations using the Fourier series representation of the piece-wise continuous magnetization density, and is shown to match FEA within 1%. The slotted stator used in the 1-MW demonstrator is modeled as a smooth iron cylinder and the windings are modeled with a surface current. Then the average torque and torque ripple produced by the machine are calculated with the Lorentz-Kelvin force density. The torque calculation in Chapter 2 runs 100,000 times faster than 2D FEA (0.6 ms vs. 44 s) and matches FEA within 1.2 percent. The models in Chapter 2 allow parameters to be swept quickly in the initial design of a machine and they provide insight into how different parameters affect machine performance.

In Chapter 3, a method for experimentally characterizing the core-loss and B-H curves of a sample lamination stack is developed and employed for various samples of iron-cobalt at different stages of the manufacturing process of the 1-MW demonstrator stator. A conventional lamination bonding process is found to increase the core loss of iron-cobalt laminations by 20% at the operating point of the 1-MW demonstrator. An alternative stator manufacturing process with no impact on core loss is identified and experimentally verified. The core loss of a stack of full-size stator laminations is found to match the core loss measured on the smaller samples used previously. Initially, a mechanical resonance of the full-size stator laminations caused artificially-high core-loss measurements, but the mechanical resonance was avoided by measuring core loss at a different frequency.

In Chapter 4, the implications of the results in the previous chapters is discussed, and further work is proposed for improving the generality of the models in Chapter 2 and the

experimental results in Chapter 3.

Chapter 2

Electromagnetic Modeling of an Electric Machine with a Halbach Array Rotor and Slotted Stator Iron

2.1 Introduction

This chapter presents a method for analytically calculating the torque produced by an electric machine with a Halbach-array rotor and slotted stator iron. In Section 2.2, the magnetic field produced by a cylindrical, segmented, Halbach array is derived from Maxwell's Equations, and matches the field calculated numerically with Finite Element Analysis (FEA) within 1%. In Section 2.3.1, a method for modeling a slotted stator as a smooth cylinder with a surface currents is explained and executed for a concentrated-wound, three-phase stator. In Section 2.3.2, the average torque and torque ripple produced by an electric machine with a Halbach array rotor and slotted stator iron are calculated using the models developed in Section 2.2 and Section 2.3.1, and the Lorentz-Kelvin force density. The torque formula developed in Section 2.3.2 matches the torque calculated with FEA within 1.2% for a real stator and computes 100,000 times faster than 2D FEA (0.56 ms vs. 44 s). As discussed in

Section 2.3, the models presented in this chapter are recommended for the initial design of electric machines with a Halbach array rotor and slotted stator iron given the advantage in computation time over FEA and insight provided into the effect of various parameters on machine performance.

Many of the modeling techniques used in this chapter have been used before to develop models for other applications. The use of Fourier series to represent the piece-wise continuous magnetization density of a segmented Halbach array in Section 2.2.1 is a common technique used to simplify the analysis of segmented Halbach arrays. For example, Song et al. (2020) used a Fourier series representation of magnetization density to calculate the performance of a machine with a Halbach array rotor and slotless stator iron [9]. The analysis of the magnetic field produced by a single harmonic of the segmented Halbach array in Section 2.2.2 follows an approach similar to that used by Xia et al. (2004) to calculate the field for a non-segmented Halbach array [10]. The modeling of a slotted stator as a smooth cylinder with a surface current in Section 2.3.1 is adapted from Dowdle (2022) [4]. However, the combination of the segmented Halbach array model in Section 2.2 with the slotted stator model in Section 2.3.1 to produce the formula for torque in Section 2.3.2 has not been published previously. Furthermore, Section 2.3 uses the models presented in this chapter to explain for the first time why, counter-intuitively, torque ripple can increase as the number of segments in the Halbach array increases.

2.2 Segmented Halbach Array Model

In this section, a closed form expression for the magnetic field produced by a cylindrical, segmented Halbach array in cylindrical coordinates is derived from Maxwell's Equations. The magnetic field in the air-gap is given in Equation (2.22).

The ideal cylindrical Halbach array has rotating magnetization density given by

$$\vec{M} = M_o \cos(p\phi)\hat{r} \pm M_o \sin(p\phi)\hat{\phi} \tag{2.1}$$

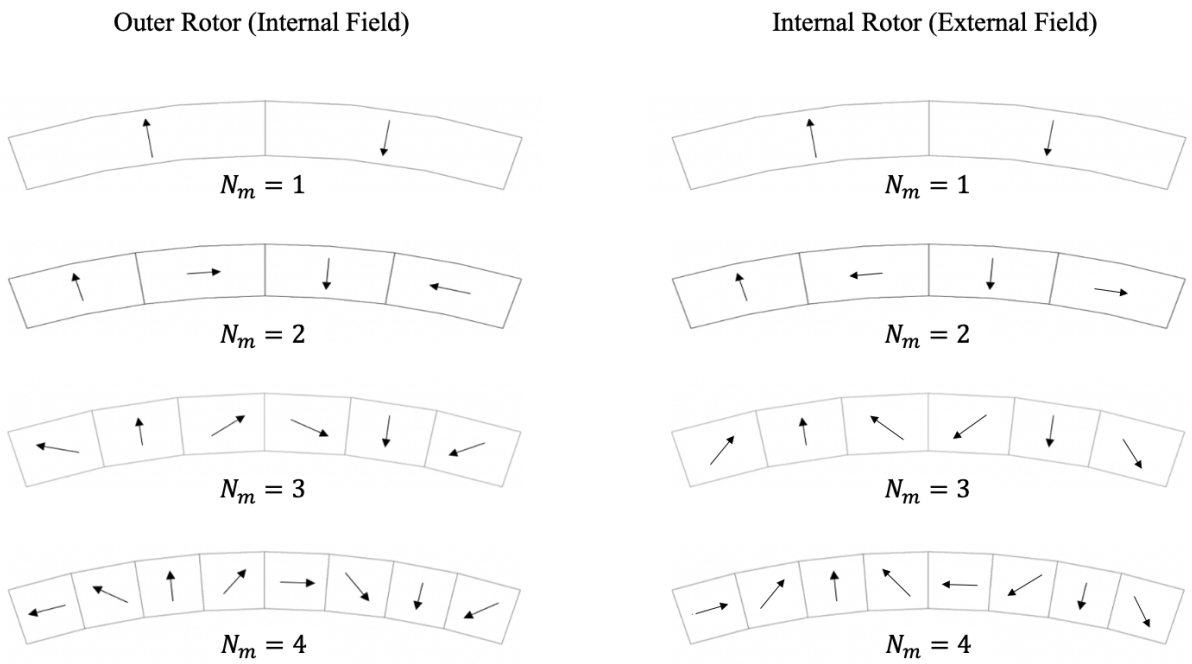

Figure 2.1: Segmented, cylindrical Halbach arrays with an increasing number of segments per pole, N_m.

where p is the number of pole pairs, and M_o is the magnitude of magnetization. In Equation (2.1), +, or forward rotating magnetization, describes an outer-rotor machine (internal field) and −, or backward rotating magnetization, describes an inner-rotor machine (external field) [10]. The ideal rotating magnetization in Equation (2.1) creates a perfectly sinusoidal magnetic field in the air-gap while cancelling the field outside the array. It is possible to manufacture a magnet with the ideal rotating magnetization in Equation (2.1) , as shown in Xia et al. (2004) [10]. However, currently the most practical and economical way to manufacture a cylindrical Halbach array is with magnet segments, cut into arcs, each with a uniform direction of magnetization given by sampling the ideal rotating magnetization. Several examples of cylindrical, segmented Halbach arrays are illustrated in Figure 2.1.

Using more magnet segments in the array allows for higher resolution sampling of the ideal rotating magnetization density, and thus results in less harmonic distortion in the air-gap field and less magnetic field outside the air-gap. However, manufacturing cost and complexity increases with the number of segments in the array, as thinner magnets and

more directions of magnetization are needed. The model presented in this section describes how increasing the number of segments per pole, N_m, changes the air-gap field (see Figure 2.8) and the torque produced by the machine (see Figure 2.22), helping to find the optimal balance between manufacturing complexity and performance.

The key idea behind the model presented in this section is representing the piece-wise continuous magnetization density of a cylindrical, segmented Halbach array as a Fourier series. For each harmonic of the magnetization density, Maxwell's Equations are solved for the magnetic field in the air-gap. All of the harmonics are superimposed to find the total magnetic field in the air-gap.

The closed form expression for the magnetic field in the air-gap given in Equation (1) matches the fields calculated numerically with FEA within 1% over a wide range of test cases and a field scan of a manufactured Halbach array rotor within the error of the experiment, as shown in Section 2.2.3.

2.2.1 Fourier Series Representation of $\vec{M}$

The uniform magnetization density for a single magnet segment, referred to as the k^{th} segment, as depicted in Figure 2.2, is defined as

$$\vec{M}_k = M_o \cos(\theta_k)\hat{x}_k + M_o \sin(\theta_k)\hat{y}_k \tag{2.2}$$

where the axes $\hat{x}_k$ and $\hat{y}_k$ are defined as parallel and perpendicular, respectively, to the center-line of the k^{th} magnet segment, and M_o, the amplitude of the magnetization density, is defined as $M_o = \frac{B_r}{\mu_0}$, where B_r is the remnant flux density, a material property of the magnets, and $\mu_0 = 4\pi * 10^{-7}$ H/m is the permeability of free space.

The direction of magnetization for the k^{th} magnet segment is given by sampling the ideal

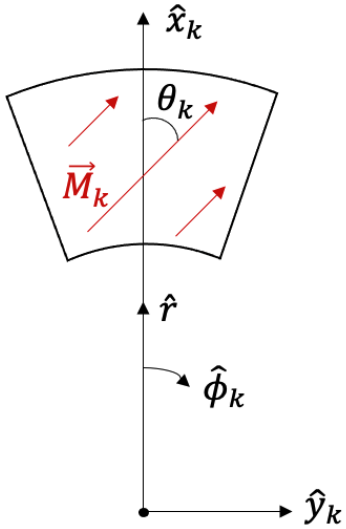

Figure 2.2: Magnetization density in the k^{th} magnet segment.

rotating magnetization density at the center-line of the segment:

$$\theta_k = \pm k\frac{\pi}{N_m} \tag{2.3}$$

where +, or forward rotating magnetization, describes an outer-rotor machine (internal field) and −, or backward rotating magnetization, describes an inner-rotor machine (external field), and k is the index of the magnet segment in the array, $k \in \{0, 1, ..., 2N_m - 1\}$ over one pole-pair.

To find the Fourier series representation of $\vec{M}$ in cylindrical coordinates, $\vec{M}_k$ in the k^{th} magnet segment must be transformed to cylindrical coordinates. The tangential axis of the k^{th} magnet segment, ϕ_k, is defined by rotating the global tangential axis, ϕ, such that the origin is at the center of the magnet:

$$\phi_k = \phi - k\Delta\phi \tag{2.4a}$$

$$\Delta\phi = \frac{\pi}{N_m p} \tag{2.4b}$$

$$\hat{\phi}_k = \hat{\phi} \tag{2.4c}$$

where $\Delta\phi$ is the angular width of a magnet segment. The coordinate transformation,

$$x_k = r\cos(\phi_k) \rightarrow \nabla x_k = \hat{x}_k = \cos(\phi_k)\hat{r} - \sin(\phi_k)\hat{\phi} \tag{2.5a}$$

$$y_k = r\sin(\phi_k) \rightarrow \nabla y_k = \hat{y}_k = \sin(\phi_k)\hat{r} + \cos(\phi_k)\hat{\phi}, \tag{2.5b}$$

applied to Equation (2.2) gives the expression for $\vec{M}_k$ in cylindrical coordinates:

$$\vec{M}_k = M_o\cos(\phi_k - \theta_k)\hat{r} - M_o\sin(\phi_k - \theta_k)\hat{\phi} \tag{2.6a}$$

$$\vec{M}_k = M_o\cos(\phi - k\frac{\pi}{pN_m} - \theta_k)\hat{r} - M_o\sin(\phi - k\frac{\pi}{pN_m} - \theta_k)\hat{\phi}. \tag{2.6b}$$

The piece-wise continuous functions $M_r(\phi)$ and $M_\phi(\phi)$ are represented as Fourier series in order to find a closed form expression for the magnetic field in the air-gap:

$$\vec{M} = M_r(\phi)\hat{r} + M_\phi(\phi)\hat{\phi} = \sum_{n=1,3,5,..}^{\infty} \alpha_n\cos(np\phi)\hat{r} + \beta_n\sin(np\phi)\hat{\phi}. \tag{2.7}$$

$M_r(\phi)$ is even and $M_\phi(\phi)$ is odd, thus only cosine and sine functions, respectively, are needed in the Fourier series. Both $M_r(\phi)$ and $M_\phi(\phi)$ are half wave anti-symmetric, therefore only odd harmonics are needed. The Fourier coefficients α_n are evaluated using the formula

$$\alpha_n = \frac{2}{T}\int_0^T M_r(\phi)\cos(np\phi)\,d\phi = \frac{4}{T}\int_0^{T/2} M_r(\phi)\cos(np\phi)\,d\phi \tag{2.8a}$$

$$T = \frac{2\pi}{p} \tag{2.8b}$$

where T is the period of the array, taking advantage of the fact that $M_r(\phi)$ is half-wave anti-symmetric. The integral in Equation (2.8a) is evaluated separately for each magnet segment and summed together to find α_n:

$$\alpha_n = \frac{2p}{\pi}\sum_{k=0}^{N_m}\int_{\phi_{ak}}^{\phi_{bk}} M_o\cos(\phi - k\frac{\pi}{pN_m} - \theta_k)\cos(np\phi)\,d\phi \tag{2.9a}$$

$$\phi_{ak} = \max(0, (k - \frac{1}{2})\Delta\phi) = \max(0, (k - \frac{1}{2})\frac{\pi}{pN_m}) \tag{2.9b}$$

$$\phi_{bk} = \min(\frac{\pi}{p}, (k + \frac{1}{2})\Delta\phi) = \min(\frac{\pi}{p}, (k + \frac{1}{2})\frac{\pi}{pN_m}). \tag{2.9c}$$

Evaluating the definite integral for α_n gives

$$\alpha_n = M_o \frac{2p}{\pi} \sum_{k=0}^{N_m} \left[\frac{\sin((np+1)\phi - k\frac{\pi}{pN_m} - \theta_k)}{2(np+1)} + \frac{\sin((np-1)\phi + k\frac{\pi}{pN_m} + \theta_k)}{2(np-1)} \right]_{\phi_{ak}}^{\phi_{bk}}. \tag{2.9d}$$

The Fourier coefficients β_n are found by following the same approach as used for α_n, resulting in

$$\beta_n = M_o \frac{2p}{\pi} \sum_{k=0}^{N_m} \left[\frac{\sin((np+1)\phi - k\frac{\pi}{pN_m} - \theta_k)}{2(np+1)} - \frac{\sin((np-1)\phi + k\frac{\pi}{pN_m} + \theta_k)}{2(np-1)} \right]_{\phi_{ak}}^{\phi_{bk}}. \tag{2.10}$$

The Fourier series formulation of $M_\phi(\phi)$ and $M_r(\phi)$ are computed using the MATLAB function listed in Appendix A for various numbers of magnet segments per pole, N_m, and numbers of pole-pairs, p, and plotted in Figure 2.3. As demonstrated in Figure 2.3, $M_\phi(\phi)$ lags $M_r(\phi)$ by 90 degrees for the outer rotor array and leads $M_r(\phi)$ by 90 degrees for the inner rotor array, creating forward and backward rotating magnetization, respectively. $M_\phi(\phi)$ and $M_r(\phi)$ are the same shape when N_m is even, but the peak of $M_\phi(\phi)$ is wider and lower than $M_r(\phi)$ when N_m is odd due to way in which the ideal rotating magnetization is sampled.

The plots of the magnitudes of the spatial harmonics of the magnetization density in Figure 2.4 illustrate that each harmonic is either rotating forward ($\alpha_n = \beta_n$) or backward ($\alpha_n = -\beta_n$) because of the way in which the ideal rotating magnetization is sampled in this section.

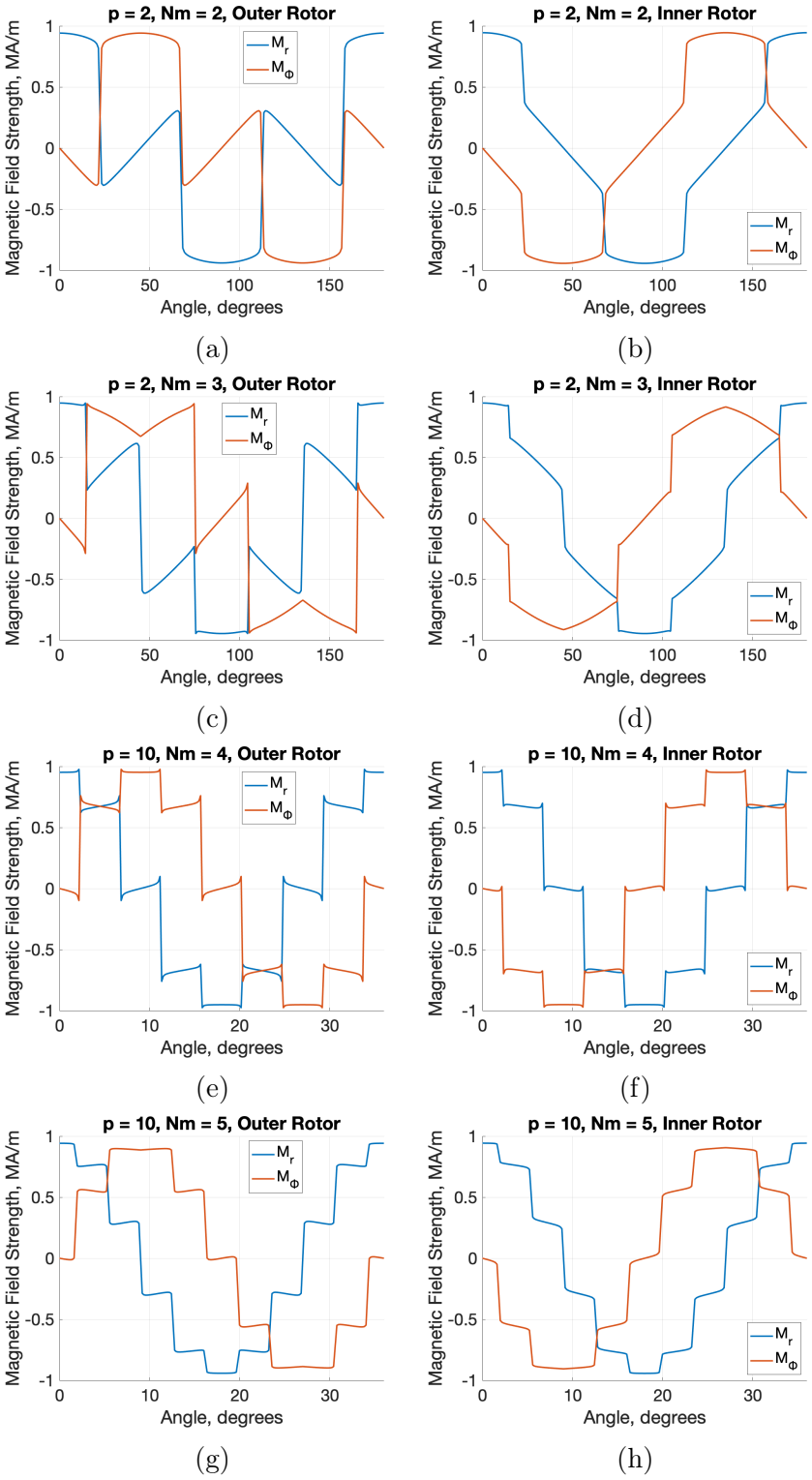

Figure 2.3: The Fourier series representations of $M_r(\phi)$ and $M_\phi(\phi)$ plotted for various different Halbach arrays.

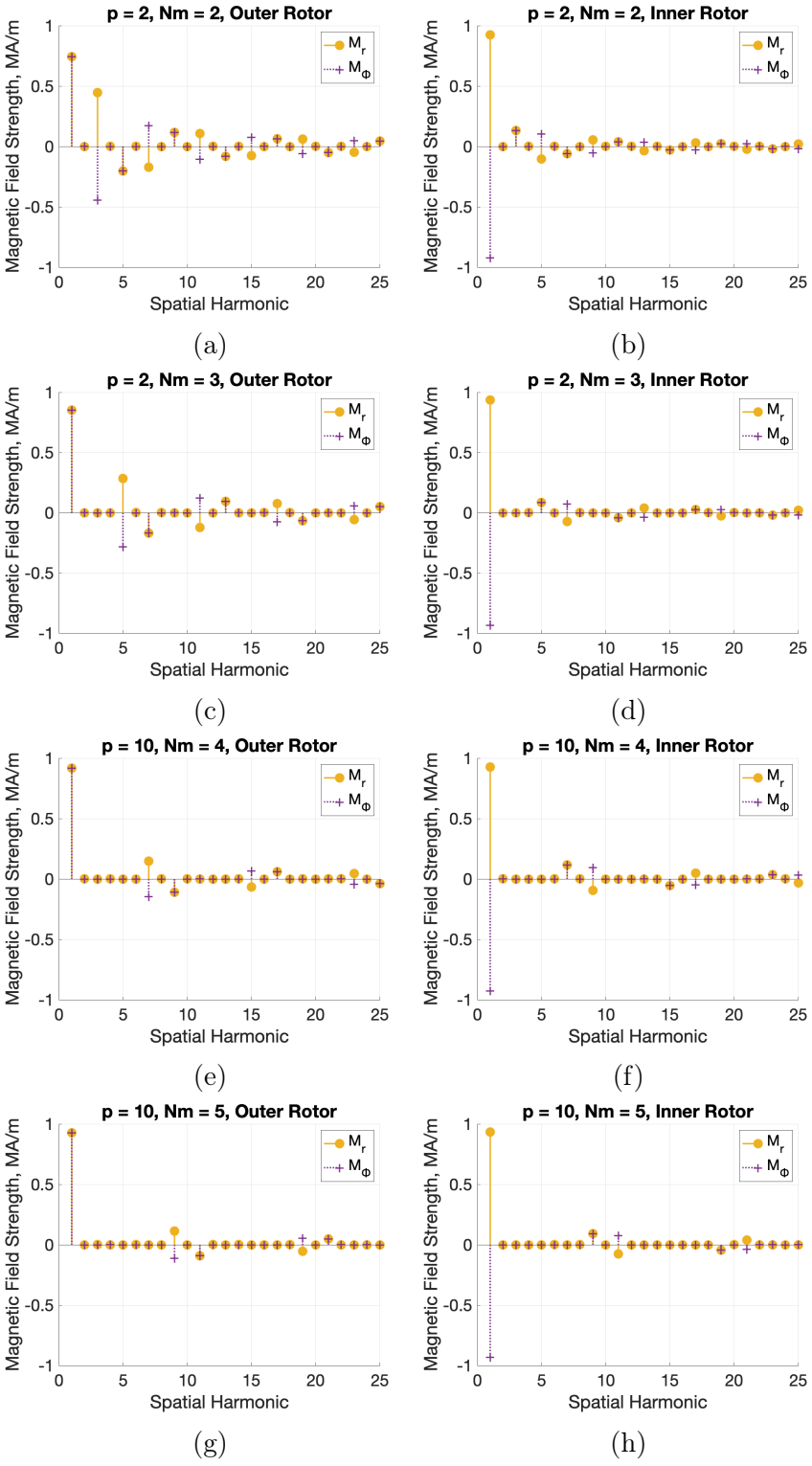

Figure 2.4: The magnitudes of the spatial harmonic of $M_r(\phi)$ and $M_\phi(\phi)$ for various different Halbach arrays.

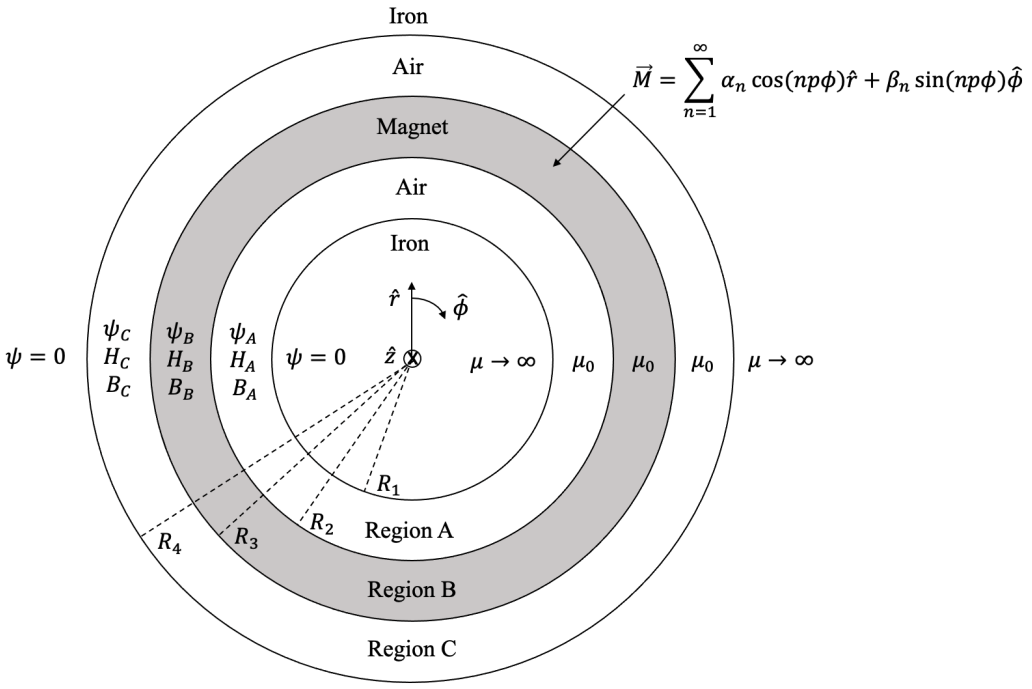

Figure 2.5: General machine architecture used for finding the air-gap field.

2.2.2 Air-gap Fields

In this section, the Fourier series formulations of $M_r(\phi)$ and $M_\phi(\phi)$ described in Section 2.2.1 are used to solve Maxwell's Equations for the magnetic field in the air-gap. There are eight common architectures of radial-flux, Halbach array machines given by the permutations of the following three parameters:

- outer rotor (external field) or inner rotor (external field);
- include stator back iron or not;
- include rotor back iron or not.

Instead of finding the air-gap field for all eight architectures separately, the magnetic field solution for the general machine shown in Figure 2.5 can be adapted to each permutation by adjusting the radii, R_1, R_2, R_3, R_4. The idea for the generalized machine architecture comes from Xia et al. (2004) [10].

Several assumptions are made for the analysis presented in this subsection.

1. The $\frac{\partial \vec{D}}{\partial t}$ term is small enough to be ignored in Ampere's law,

$$\nabla \times \vec{H} = \vec{J}_f + \frac{\partial \vec{D}}{\partial t} = \vec{J}_f. \tag{2.11}$$

2. The permeability of iron is infinite, $\mu \to \infty$, and therefore $\vec{H} = 0$ and the magnetic scalar potential ψ is constant in the iron.

3. The magnet region has the relative permeability $\mu_r = 1$.

4. The stator iron is smooth, and the effect of stator slots is ignored.

Assumption 1 is valid as long as the active region of the machine is much smaller than the wavelength of light at the electrical frequency of the machine. Assumption 2 is valid if the iron in the machine does not saturate. In Section 2.2.4, Assumption 3 is shown to be acceptable for magnets when $\mu_r = 1.05$, but when $\mu_r = 1.2$ there is an 8% percent error between the model and FEA. Assumption 4 will not impact the torque calculation in Section 2.3.2 as long as the stator slot openings are small enough to be ignored at some point in the air-gap, not necessarily at the stator surface, as explained in Section 2.2.4.

The magnetic fields in the air-gaps of the machine in Figure 2.5 are found using the magnetic scalar potential, ψ. The magnetic fields sourced by each harmonic of $\vec{M}$ are found separately and then superimposed to get the total magnetic field. The fields from each harmonic can be superimposed because the iron is assumed to be linear, $\mu \to \infty$.

The stator currents are ignored in this section, and in Section 2.3 the stator currents are superimposed on the magnetic field found in this section to find the torque produced by the machine. Ampere's law under Assumption 1 (commonly referred to as the magneto-quasistatic approximation), given that $\vec{J}_f = 0$ in every region in Figure 2.5, takes the form

$$\nabla \times \vec{H} = 0, \tag{2.12a}$$

and is satisfied if

$$\vec{H} = -\nabla\psi \tag{2.12b}$$

where ψ is any scalar valued function. ψ is referred to as the magnetic scalar potential.

Substituting the constitutive law for magnetization,

$$\vec{B} = \mu_0 \left(\vec{H} + \vec{M}\right) \tag{2.13}$$

where $\vec{B}$ is the magnetic flux density, $\vec{H}$ is the magnetic field, and $\vec{M}$ is the magnetization density, into Gauss's law for magnetic fields,

$$\nabla \cdot \vec{B} = 0, \tag{2.14}$$

results in Laplace's Equation in Region A and Region C in Figure 2.5, where $\vec{M} = 0$,

$$\nabla^2\psi_A = \nabla^2\psi_C = \nabla \cdot \vec{M} = 0, \tag{2.15}$$

and Possion's Equation in Region B,

$$\nabla^2\psi_B = \nabla \cdot \vec{M}_n = \frac{1}{r}\frac{\partial(rM_{nr})}{\partial r} + \frac{1}{r}\frac{\partial M_{n\phi}}{\partial \phi} = (\alpha_n + np\beta_n)\frac{1}{r}\cos(np\phi). \tag{2.16}$$

Although the scalar potentials, ψ_A, ψ_B, and ψ_C are unique for every harmonic, the n subscript is omitted to simplify notation.

The method of particular and homogeneous solutions is used to find the function ψ_B that satisfies Poisson's Equation (2.16) and the boundary conditions in Equation (2.18):

$$\psi_B = \psi_{Bp} + \psi_{Bh} \tag{2.17a}$$

where ψ_{Bp} is any particular solution that satisfies Poisson's Equation (2.16), such as

$$\psi_{Bp} = \frac{(\alpha_n + np\beta_n)}{1-(np)^2} r\cos(np\phi), \tag{2.17b}$$

which was obtained by guessing and checking the solution, and ψ_{Bh} is any homogeneous solution that satisfies Laplace's equation,

$$\nabla^2 \psi_{Bh} = 0 \tag{2.17c}$$

and helps ψ_B satisfy the boundary conditions in Equation (2.18).

The boundary conditions for the generalized machine in Figure 2.5 are

1. Ampere's Law at $r = R_1$:

$$\hat{r} \times \left[\vec{H}_A - 0\right] = \vec{K}_f = 0 \tag{2.18a}$$

2. Gauss's Law at $r = R_2$:

$$\hat{r} \cdot \left[\vec{H}_B - \vec{H}_A\right] = -\hat{r} \cdot \left[\vec{M}_B - \vec{M}_A\right] = -\alpha_n \cos(np\phi) \tag{2.18b}$$

3. Ampere's Law at $r = R_2$:

$$\hat{r} \times \left[\vec{H}_B - \vec{H}_A\right] = \vec{K}_f = 0 \tag{2.18c}$$

4. Gauss's Law at $r = R_3$:

$$\hat{r} \cdot \left[\vec{H}_C - \vec{H}_B\right] = -\hat{r} \cdot \left[\vec{M}_C - \vec{M}_B\right] = \alpha_n \cos(np\phi) \tag{2.18d}$$

5. Ampere's Law at $r = R_3$:

$$\hat{r} \times \left[\vec{H}_C - \vec{H}_B\right] = \vec{K}_f = 0 \tag{2.18e}$$

6. Ampere's Law at $r = R_4$:

$$\hat{r} \times \left[0 - \vec{H}_C\right] = \vec{K}_f = 0 \tag{2.18f}$$

To satisfy Boundary Condition 1 and Laplace's Equation (2.15), let

$$\psi_A = A\left(r^{np} - R_1^{2np} r^{-np}\right)\cos(np\phi) \tag{2.19a}$$

where A is a constant found by satisfying the remaining boundary conditions.

To satisfy Boundary Condition 6 and Laplace's Equation (2.15), let

$$\psi_C = C\left(r^{-np} - R_4^{-2np} r^{np}\right)\cos(np\phi) \tag{2.19b}$$

where C is a constant found by satisfying the remaining boundary conditions.

To satisfy Boundary Condition 2 through Boundary Condition 5 and Poisson's Equation (2.16), let

$$\psi_B = \left(B_1 r^{np} + B_2 r^{-np}\right)\cos(np\phi) + \frac{(\alpha_n + np\beta_n)}{1-(np)^2} r\cos(np\phi) \tag{2.19c}$$

where B_1 and B_2 are constants found by satisfying the remaining boundary conditions.

Substituting Equation (2.19) into the boundary conditions in Equation (2.18) results in four equations with four unknown constants, A, B_1, B_2, and C as follows.

1. Boundary Condition 2 (Gauss's Law at $r = R_2$):

$$A\left(R_2^{np-1} + R_1^{2np} R_2^{-np-1}\right) - B_1 R_2^{np-1} + B_2 R_2^{-np-1} = \frac{(np\alpha_n + \beta_n)}{1-(np)^2} \tag{2.20a}$$

2. Boundary Condition 3 (Faraday's Law at $r = R_2$):

$$A\left(R_2^{np-1} - R_1^{2np} R_2^{-np-1}\right) - B_1 R_2^{np-1} - B_2 R_2^{-np-1} = \frac{(np\alpha_n + \beta_n)}{1-(np)^2} \tag{2.20b}$$

3. Boundary Condition 4 (Gauss's Law at $r = R_3$):

$$C\left(R_3^{-np-1} + R_4^{-2np}R_3^{np-1}\right) + B_1R_3^{np-1} - B_2R_3^{-np-1} = -\frac{(np\alpha_n + \beta_n)}{1-(np)^2} \tag{2.20c}$$

4. Boundary Condition 5 (Faraday's Law at $r = R_3$):

$$-C\left(R_3^{-np-1} - R_4^{-2np}R_3^{np-1}\right) + B_1R_3^{np-1} + B_2R_3^{-np-1} = -\frac{(np\alpha_n + \beta_n)}{1-(np)^2} \tag{2.20d}$$

Solving the system in Equation (2.20) for A, B_1, B_2, and C gives

$$A = \frac{1}{1-\left(\frac{R_1}{R_4}\right)^{2np}}\left[\frac{1}{2}\frac{(\alpha_n+\beta_n)}{(1-np)}\left(R_2^{1-np} - R_3^{1-np}\right)\right.$$
$$\left. + \frac{1}{2}\frac{(-\alpha_n+\beta_n)}{(1+np)}\left(\left(\frac{R_3}{R_4}\right)^{2np}R_3^{1-np} - \left(\frac{R_2}{R_4}\right)^{2np}R_2^{1-np}\right)\right] \tag{2.21a}$$

$$B_1 = \frac{1}{1-\left(\frac{R_1}{R_4}\right)^{2np}}\left[\frac{1}{2}\frac{(\alpha_n+\beta_n)}{(1-np)}\left(\left(\frac{R_1}{R_4}\right)^{2np}R_2^{1-np} - R_3^{1-np}\right)\right.$$
$$\left. + \frac{1}{2}\frac{(-\alpha_n+\beta_n)}{(1+np)}\left(\left(\frac{R_3}{R_4}\right)^{2np}R_3^{1-np} - \left(\frac{R_2}{R_4}\right)^{2np}R_2^{1-np}\right)\right] \tag{2.21b}$$

$$B_2 = \frac{1}{1-\left(\frac{R_1}{R_4}\right)^{2np}}\left[\frac{1}{2}\frac{(-\alpha_n+\beta_n)}{(1+np)}\left(R_2^{1+np} - \left(\frac{R_1}{R_4}\right)^{2np}R_3^{1+np}\right)\right.$$
$$\left. + \frac{1}{2}\frac{(\alpha_n+\beta_n)}{(1-np)}\left(\left(\frac{R_1}{R_3}\right)^{2np}R_3^{1+np} - \left(\frac{R_1}{R_2}\right)^{2np}R_2^{1+np}\right)\right] \tag{2.21c}$$

$$C = \frac{1}{1-\left(\frac{R_1}{R_4}\right)^{2np}}\left[\frac{1}{2}\frac{(-\alpha_n+\beta_n)}{(1+np)}\left(R_2^{1+np}-R_3^{1+np}\right)\right.$$
$$\left.+\frac{1}{2}\frac{(\alpha_n+\beta_n)}{(1-np)}\left(\left(\frac{R_1}{R_3}\right)^{2np}R_3^{1+np}-\left(\frac{R_1}{R_2}\right)^{2np}R_2^{1+np}\right)\right]. \quad (2.21d)$$

Applying the definition of the scalar potential, Equation (2.12b), to Equation (2.19) and superimposing all of the harmonics together results in the magnetic fields in the air-gaps as follows.

1. For outer rotor machines (internal field):

$$H_{Ar}(r,\phi) = \sum_{n=1}^{\infty}\frac{\frac{1}{2}np}{1-\left(\frac{R_1}{R_4}\right)^{2np}}\left[\frac{(\alpha_n+\beta_n)}{(1-np)}\left(\left(\frac{r}{R_2}\right)^{np-1}-\left(\frac{r}{R_3}\right)^{np-1}\right)\right.$$
$$\left.+\frac{(\alpha_n-\beta_n)}{(1+np)}\left(\left(\frac{R_2}{R_4}\right)^{2np}\left(\frac{r}{R_2}\right)^{np-1}-\left(\frac{R_3}{R_4}\right)^{2np}\left(\frac{r}{R_3}\right)^{np-1}\right)\right]\left[1+\left(\frac{R_1}{r}\right)^{2np}\right]\cos(np\phi) \quad (2.22a)$$

$$H_{A\phi}(r,\phi) = \sum_{n=1}^{\infty}\frac{\frac{1}{2}np}{1-\left(\frac{R_1}{R_4}\right)^{2np}}\left[\frac{(\alpha_n+\beta_n)}{(1-np)}\left(\left(\frac{r}{R_2}\right)^{np-1}-\left(\frac{r}{R_3}\right)^{np-1}\right)\right.$$
$$\left.+\frac{(\alpha_n-\beta_n)}{(1+np)}\left(\left(\frac{R_2}{R_4}\right)^{2np}\left(\frac{r}{R_2}\right)^{np-1}-\left(\frac{R_3}{R_4}\right)^{2np}\left(\frac{r}{R_3}\right)^{np-1}\right)\right]\left[1-\left(\frac{R_1}{r}\right)^{2np}\right]\sin(np\phi) \quad (2.22b)$$

2. For inner rotor machines (external field):

$$H_{Cr}(r,\phi) = \sum_{n=1}^{\infty} \frac{\frac{1}{2}np}{1-\left(\frac{R_1}{R_4}\right)^{2np}} \left[\frac{(\alpha_n - \beta_n)}{(1+np)} \left(\left(\frac{R_3}{r}\right)^{1+np} - \left(\frac{R_2}{r}\right)^{1+np} \right) \right.$$
$$\left. + \frac{(\alpha_n + \beta_n)}{(1-np)} \left(\left(\frac{R_1}{R_3}\right)^{2np} \left(\frac{R_3}{r}\right)^{1+np} - \left(\frac{R_1}{R_2}\right)^{2np} \left(\frac{R_2}{r}\right)^{1+np} \right) \right] \left[1 + \left(\frac{r}{R_4}\right)^{2np} \right] \cos(np\phi) \tag{2.22c}$$

$$H_{C\phi}(r,\phi) = \sum_{n=1}^{\infty} \frac{\frac{1}{2}np}{1-\left(\frac{R_1}{R_4}\right)^{2np}} \left[\frac{(\alpha_n - \beta_n)}{(1+np)} \left(\left(\frac{R_3}{r}\right)^{1+np} - \left(\frac{R_2}{r}\right)^{1+np} \right) \right.$$
$$\left. + \frac{(\alpha_n + \beta_n)}{(1-np)} \left(\left(\frac{R_1}{R_3}\right)^{2np} \left(\frac{R_3}{r}\right)^{1+np} - \left(\frac{R_1}{R_2}\right)^{2np} \left(\frac{R_2}{r}\right)^{1+np} \right) \right] \left[1 - \left(\frac{r}{R_4}\right)^{2np} \right] \sin(np\phi) \tag{2.22d}$$

where α_n is defined in Equation (2.9d) and β_n is defined in Equation (2.10).

In the absence of rotor back iron ($R_1 = 0$ for inner rotor machines and $R_4 = \infty$ for outer rotor machines), Equation (2.22) reveals that forward rotating harmonics of magnetization density ($\alpha_n = \beta_n$) create sinusoidal fields internally and no field externally, whereas backward rotating harmonics of magnetization density ($\alpha_n = -\beta_n$) create sinusoidal fields externally and no field internally.

The presence of rotor back iron has two effects, as seen in Equation (2.22) and illustrated in Figure 2.7 and Figure 2.8.

1. If stator back iron is present, then rotor back iron increases the strength of every harmonic of the air-gap field.

2. For outer rotor machines, rotor back iron causes backward rotating harmonics of the magnetization density ($\alpha_n = -\beta_n$) to contribute to the internal field, and for inner rotor machines, rotor back iron causes forward rotating harmonics of the magnetization

density ($\alpha_n = \beta_n$) to contribute to the external field.

Section 2.3.2 shows that the average torque of a machine is proportional to the fundamental component of the rotor field and that higher harmonics of the rotor field cause torque ripple. Therefore, effect 1 causes an increase in both average torque and torque ripple, and effect 2 can only cause an increase in torque ripple.

The presence of stator iron ($R_1 \neq 0$ for outer-rotor machines and $R_4 \neq \infty$ for inner-rotor machines) causes the radially-directed component of the magnetic field in the air-gap to increase while causing the tangentially-directed field to decrease, as seen in Equation (2.22) and illustrated in Figure 2.7 and Figure 2.8. Intuitively, this effect is explained by the stator iron guiding the magnetic flux sourced by the Halbach array. Section 2.3.2 shows that the torque of a machine is proportional to the radially-directed component of the rotor field and independent of the tangentially-directed component of the rotor field, thus the presence of stator iron increases the torque the machine.

Equation (2.22) reveals that the presence of stator iron has a larger effect for slower rotating fields (when n and p are small), and a smaller effect on faster rotating fields (when n and p are large). This trend matches intuition, since stator iron contributes less effective steel to the magnetic circuit as the field rotates faster in space.

2.2.3 Model Validation

The fields calculated with Equation (2.22), using the MATLAB function in Appendix A, were plotted against the fields calculated numerically with FEA in Figure 2.7 and 2.8. The fields calculated with Equation (2.22) match the fields calculated with FEA to within 1%. The four different machines used to compare the model with FEA are shown in Figure 2.6. The magnets used to calculate the fields in FEA have a low relative permeability, $\mu_r = 1.05$. The fields are calculated with FEA for a higher relative permeability magnet, $\mu_r = 1.2$, and compared with Equation (2.22) in Section 2.2.4.

The mesh used to calculate the fields in FEA is shown in Figure 2.9. Reducing the element

size to half of those shown in Figure 2.9 has a negligible impact on the fields, therefore the mesh size is sufficiently small.

As discussed in Section 2.4, a Halbach array rotor with four magnet segments per pole, $N_m = 4$, ten pole-pairs, $p = 10$, and no rotor back iron was selected for use in the 1-MW demonstrator machine based on the results from the models described in this chapter. A titanium rim is used to retain the magnets, due to the high centrifugal forces at the operational speed, 12,500 rpm.

The Halbach array rotor for the 1-MW demonstrator was successfully manufactured, as seen in Figure 2.10. Recoma 35E SmCo magnets ($B_r = 1.19$ T, $\mu_r = 1.05$) were selected for their superior performance at high temperature over comparable NdFeB magnets [11]. The magnets in the rotor in Figure 2.10 are laminated axially using 64 pieces to reduce eddy current loss [4].

The rotor manufacturer performed a scan of the radial magnetic flux density with a Gauss-meter for the two manufactured rotors used in the two prototype machines. The field scan data is consistent to within 5% over all 360 degrees, measured at five different axial locations (referred to as rows) for each rotor, as shown in Figure 2.11. The 5% error could be caused by movement of the Gauss-meter probe, movement of the rotor, variation in magnet strength, or error in the Gauss-meter. The field calculated with Equation (2.22) matches the field scan measurements to within the 5% error of the measurement data, as demonstrated in Figure 2.12.

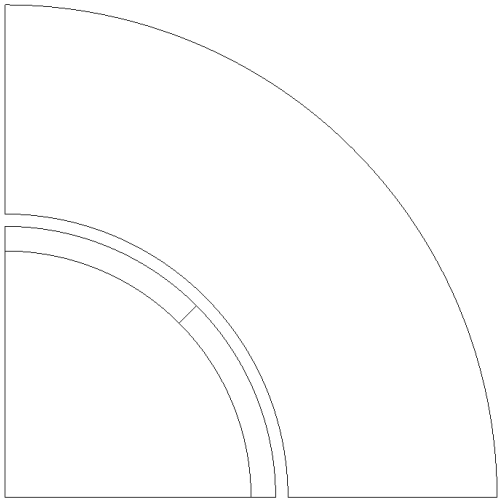

(a) Inner rotor, $p = 2$, $N_m = 2$, $R_1 = R_2 = 10$ mm, $R_3 = 11$ mm, $R_4 = 11.5$ mm

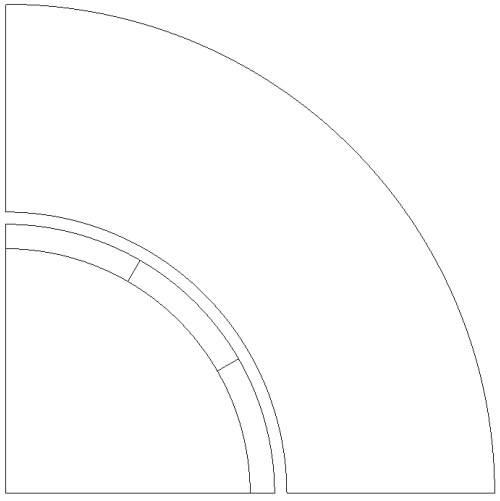

(b) Inner rotor, $p = 2$, $N_m = 3$, $R_1 = R_2 = 10$ mm, $R_3 = 11$ mm, $R_4 = 11.5$ mm

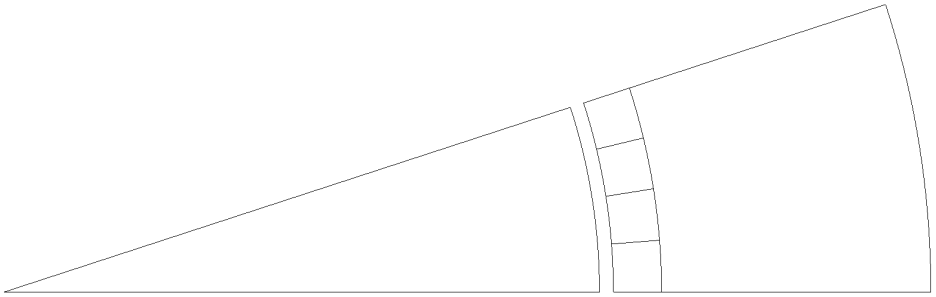

(c) Outer rotor, $p = 10$, $N_m = 4$, $R_1 = 128.5$ mm, $R_3 = 131.5$ mm, $R_3 = R_4 = 141.8$ mm

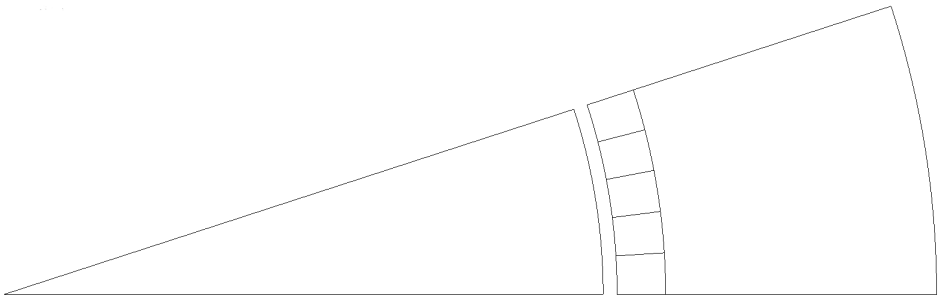

(d) Outer rotor, $p = 10$, $N_m = 5$, $R_1 = 128.5$ mm, $R_3 = 131.5$ mm, $R_3 = R_4 = 141.8$ mm

Figure 2.6: The four different Halbach array machines used to compare the model with FEA.

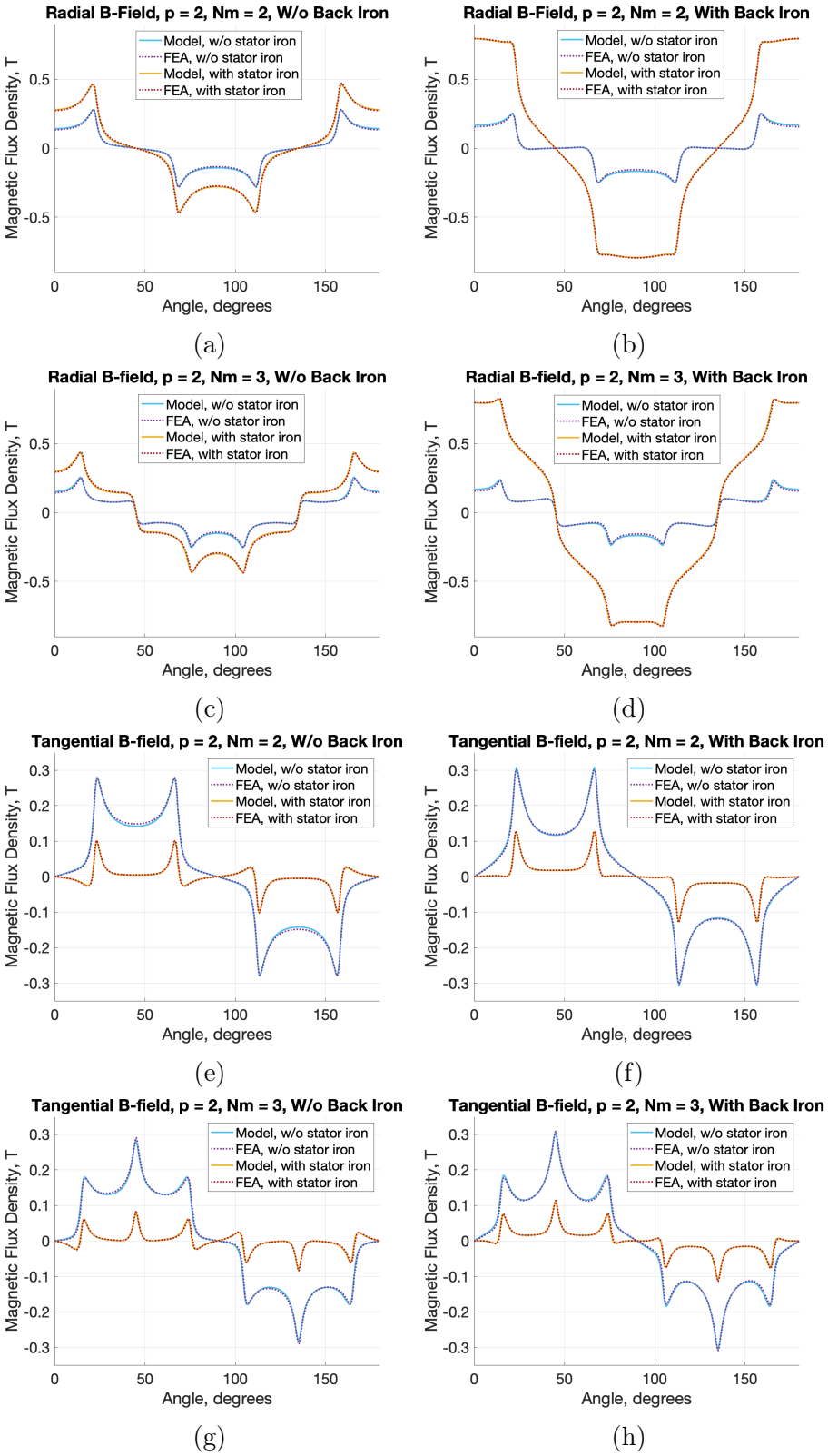

Figure 2.7: Model matches FEA to within 1% for an inner-rotor machine with two pole pairs and two and three segments per pole ($R_2 = 10$ mm, $R_3 = 11$ mm, $R_4 = 11.5$ mm, $R_{measured} = 11.25$ mm, $B_r = 1.19$ T).

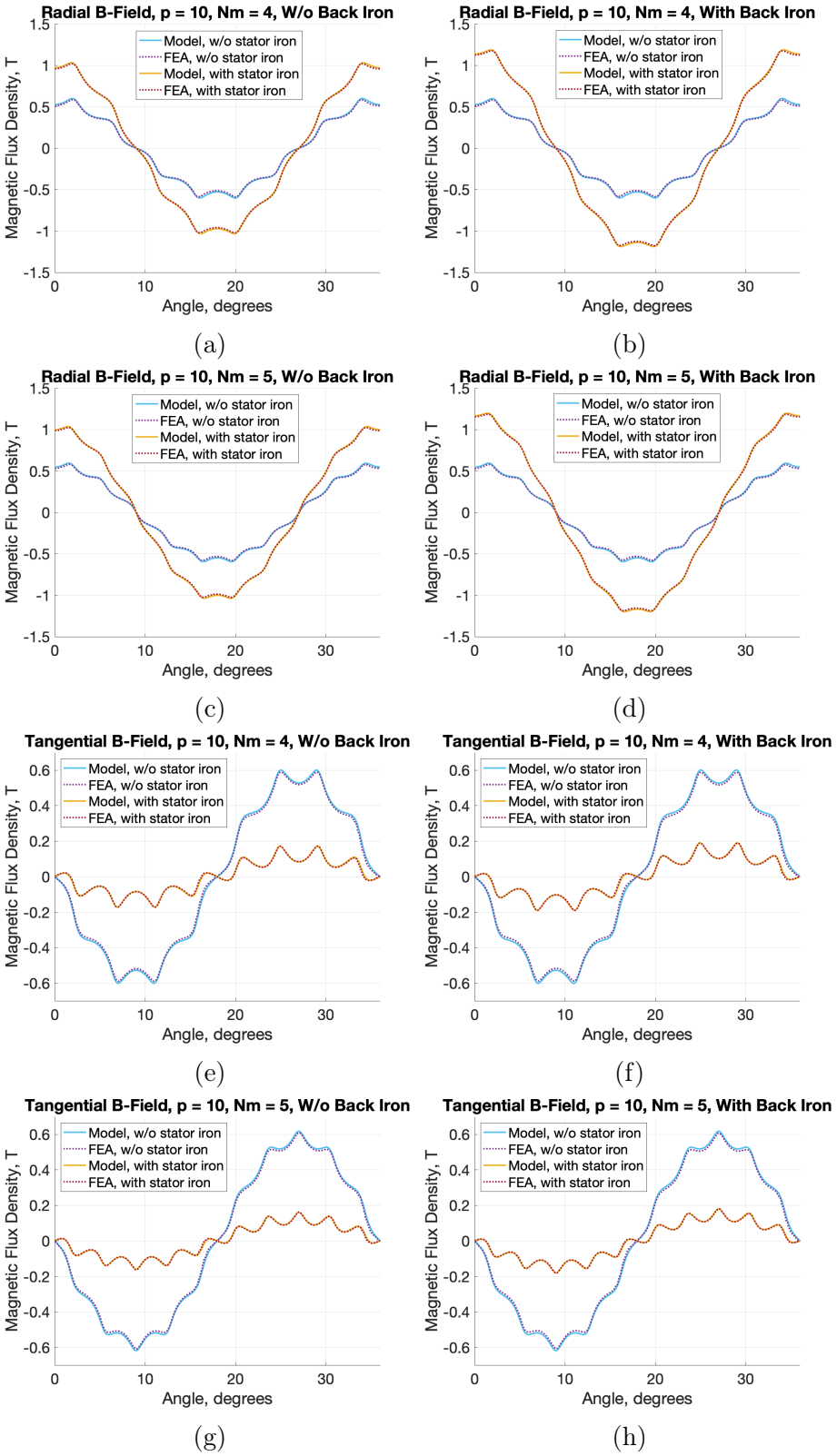

Figure 2.8: Model matches FEA within 1% for an outer-rotor machine with ten pole pairs and four and five segments per pole ($R_1 = 128.5$ mm, $R_2 = 131.5$ mm, $R_3 = 141.8$ mm, $R_{measured} = 130$ mm, $B_r = 1.19$ T).

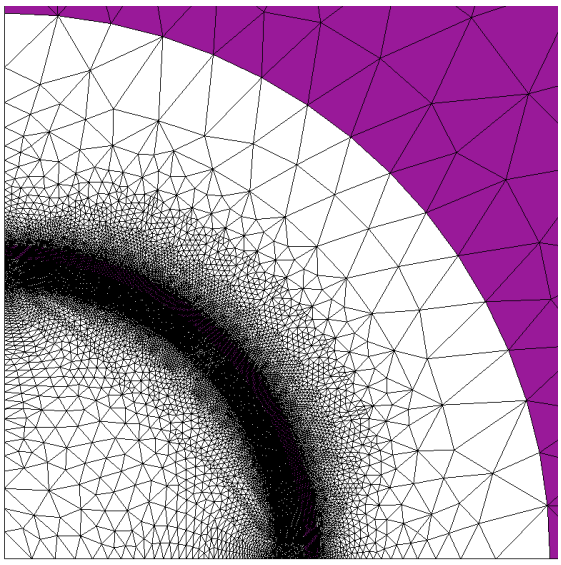

(a) Inner rotor, $p = 2$, $N_m = 2\,\&\,3$, $R_1 = R_2 = 10$ mm, $R_3 = 11$ mm, $R_4 = 11.5$ mm

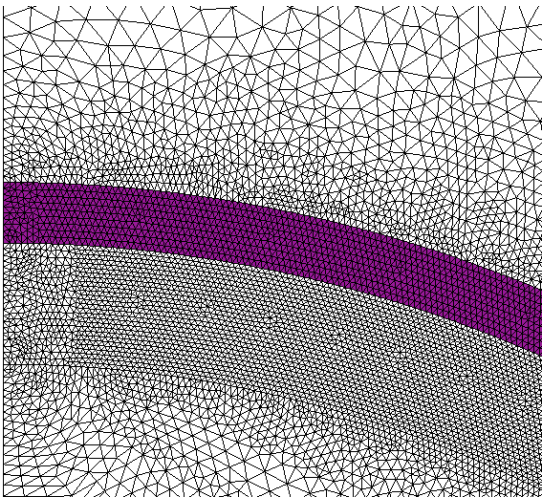

(b) Zoomed in view of (a) at the air-gap

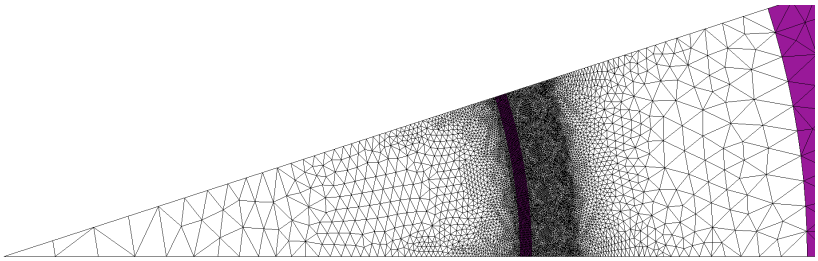

(c) Outer rotor, $p = 10$, $N_m = 4\,\&\,5$, $R_1 = 128.5$ mm, $R_3 = 131.5$ mm, $R_3 = R_4 = 141.8$ mm

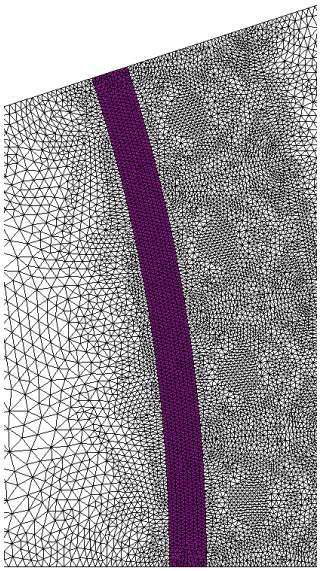

(d) Zoomed in view of (c) at the air-gap

Figure 2.9: Mesh element size used to calculate rotor fields with FEA.

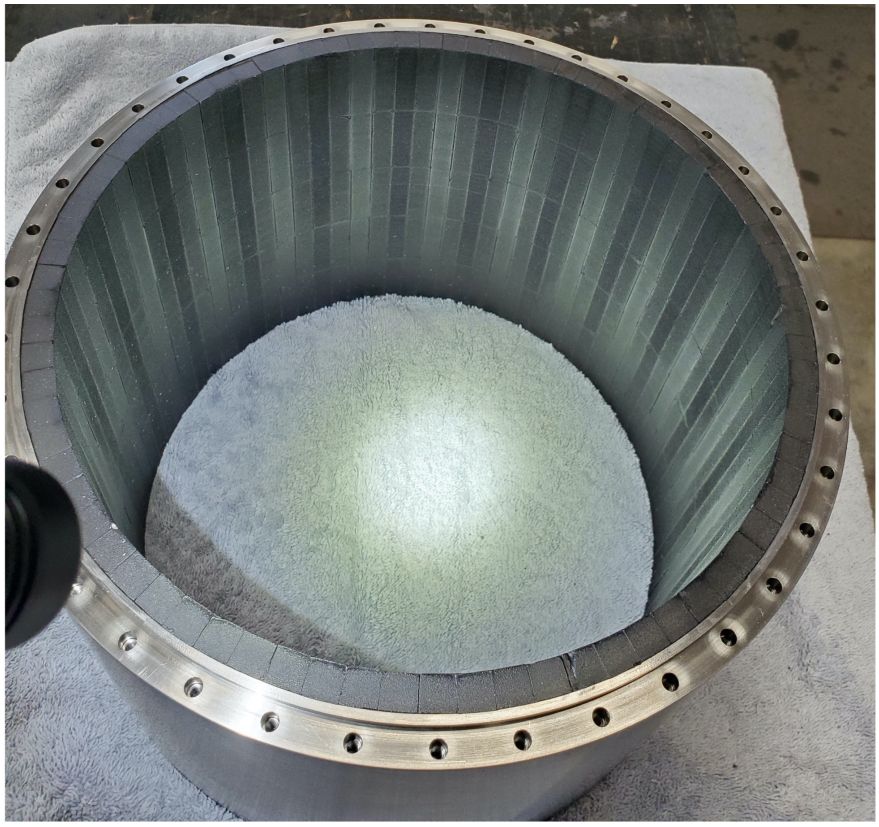

Figure 2.10: Manufactured Halbach array rotor with titanium rim to retain magnets instead of rotor back iron.

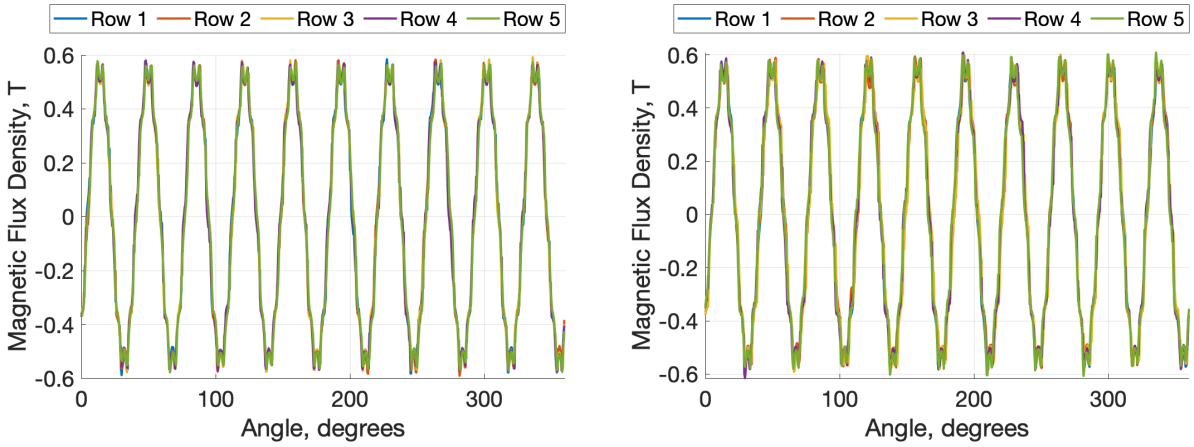

(a) Rotor 1 radial B-field scan data

(b) Rotor 2 radial B-Field scan data

Figure 2.11: Radial B-field scan data of the two manufactured rotors is consistent within 5% across all 10 pole pairs and 5 different axial locations.

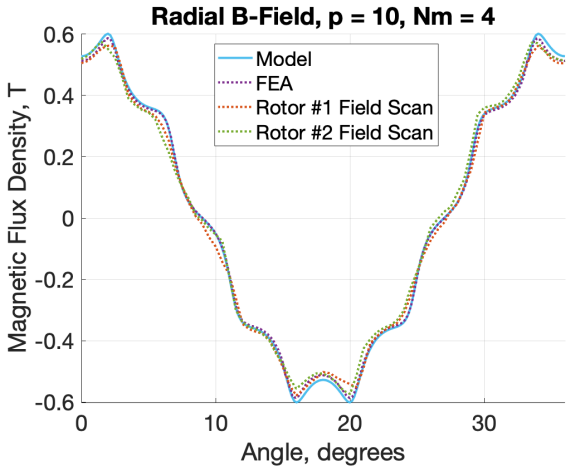

Figure 2.12: Model matches Gauss-meter field scan of manufactured rotors within 5% error of experimental setup ($R_2 = 131.5$ mm, $R_3 = 141.8$ mm, no stator iron or rotor back iron, $B_r = 1.19$ T).

2.2.4 Model Assumptions

The analysis performed in Section 2.2.2 assumes that the magnet region has the relative permeability $\mu_r = 1$. The fields labeled "FEA" in Figure 2.7 and Figure 2.8 are calculated using magnets with $\mu_r = 1.05$, and they match the model to within 1%. However, the fields labeled "FEA" in Figure 2.13 are calculated using magnets with $\mu_r = 1.2$, and there is an 8% error between the model the numerically calculated fields. These results suggest that the assumption, $\mu_r = 1$ in the magnet array, is accurate for magnets where $\mu_r \approx 1.05$, but for magnets where $\mu_r \geq 1.2$, the permeability of the magnet region should be considered in the analysis in Section 2.2.2.

Considering the relative permeability of the magnet region as a variable, the air-gap fields are calculated for a single harmonic of the magnetization density in Xia et al. (2004) [10]. This solution could be adapted to the analysis in Section 2.2.2.

The analysis performed in Section 2.2.2 assumes that the stator iron is a smooth circle, whereas, for the 1-MW demonstrator and many other machines, the stator iron has a winding embedded in slot sections. Slot sections in the stator can significantly impact the magnetic field in the air-gap near the stator iron. However, the shear force on the rotor, and thus the

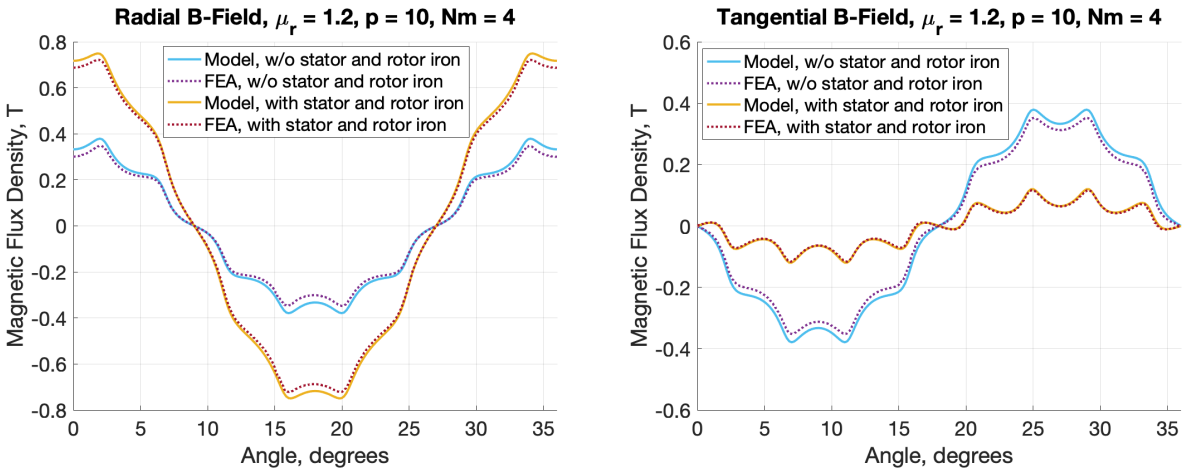

(a) (b)

Figure 2.13: Model deviates from FEA by up to 8% for magnets with high relative permeability, $\mu_r = 1.2$ (Outer rotor, $R_1 = 128.5$ mm, $R_2 = 131.5$ mm, $R_3 = 141.8$ mm, $R_{measured} = 130$ mm, $B_r = 0.75$ T).

torque of the machine, can be evaluated using the stress tensor at any radius in the air-gap,

$$f_\phi = \oiint \mu_0 H_\phi H_r \, da. \tag{2.23}$$

Therefore, as long as the magnetic field is not significantly impacted by the stator slot sections at some radius in the air-gap, the slotted stator can be modeled as a smooth cylinder without affecting the torque calculation performed in Section 2.3.2.

The air-gap field of the machine with the slotted stator shown in Figure 2.14d, calculated with FEA, matches the model to within 1% when measured far from the stator iron slots, as shown in Figure 2.14. As a result, the torque calculated in Section 2.3.2, which uses the rotor fields calculated in Section 2.2.2 assuming the stator iron is a smooth cylinder, matches with the torque calculated with FEA for the machine with the slotted stator in Figure 2.14d as shown in Section 2.3.3.

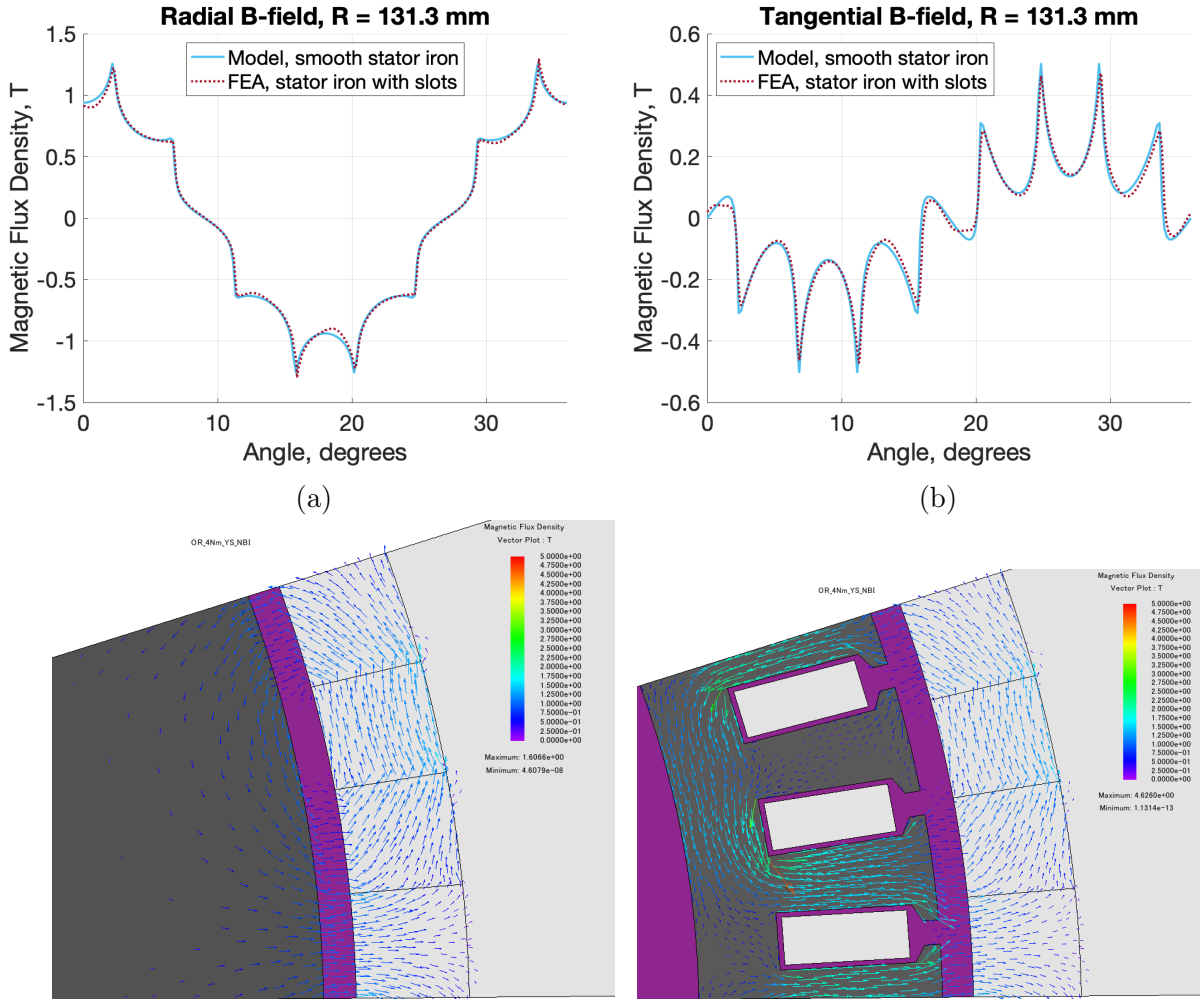

(a) (b)

(c) Vector plot of $\vec{B}$ for smooth stator (d) Vector plot of $\vec{B}$ for slotted stator

Figure 2.14: Air-gap field from model matches field calculated with FEA using a slotted stator to within 1%, far from slot sections: $R_{measured} = 131.3$ mm (width of slot opening: 2.5 mm).

2.3 Slotted Stator Model and Torque Calculation

In order to calculate the torque of an electric machine using the expression for the Halbach array rotor field developed in Section 2.2, a method of modeling a slotted stator as a smooth steel cylinder with a surface current is presented and executed for a concentrated-wound, three-phase stator in Section 2.3.1. The torque on the stator surface current from the rotor field is calculated with the Lorentz force density in Section 2.3.2. In Section 2.3.3, the torque

calculated in Section 2.3.2 is shown to match FEA to within 1.2% percent.

2.3.1 Slotted Stator Model

In a slotted stator, the magnetic flux is guided through the stator steel, around the winding, as demonstrated in Figure 2.14d. As a result, the current-carrying winding could be anywhere in the slot without changing the flow of magnetic flux in the stator iron or the magnetic field in the air-gap. The slot sections in Figure 2.15 have undefined boundaries to illustrate this point. Utilizing this observation, the winding is modeled as a surface current on the surface of the stator, where the rotor fields are known from Section 2.2. The slotted stator iron is modeled as a smooth circle of steel, which, as explained in Section 2.2.4, does not impact the torque calculation as long as the slots are small enough to be ignored at some point in the air-gap.

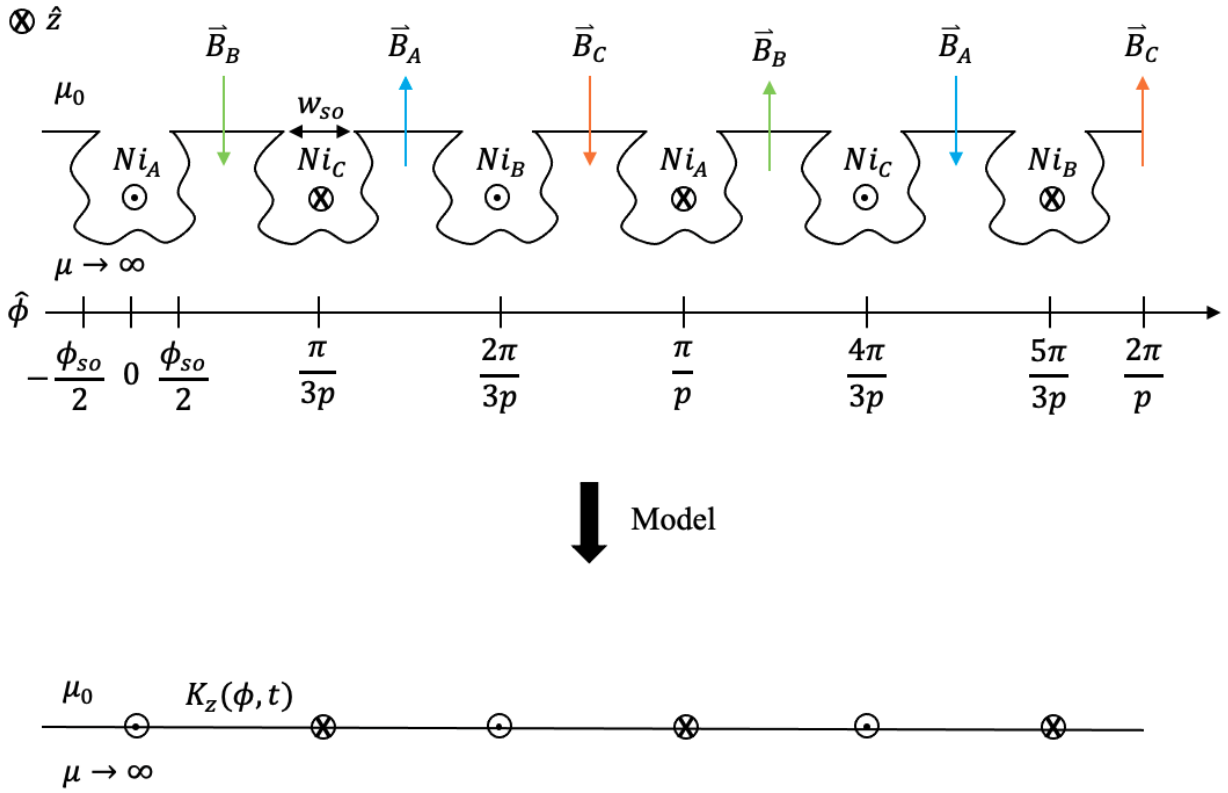

Figure 2.15: Concentrated-wound, three-phase slotted stator modeled as a smooth steel cylinder with a surface currents.

The winding in a slotless or air-cored stator cannot be modeled as a surface current because the air-gap field is dependent on the position of the winding. Song et al. (2020) demonstrates one way to determine the air-gap field and torque of a slotless Halbach array machine [9].

The following equations in this section are applied specifically for the concentrated-wound, three-phase stator illustrated in Figure 2.15. However, the same approach works for modelling distributed-wound stators, as well as stators with any number of phases. The stator in Figure 2.15 could belong to an inner or outer rotor machine.

The three magnetic axes of the stator, labeled as $\vec{B}_A$, $\vec{B}_B$, and $\vec{B}_C$ in Figure 2.15, are equally spaced apart. $\vec{B}_B$ is $\frac{2\pi}{3p}$ radians after $\vec{B}_A$, and $\vec{B}_C$ is $\frac{2\pi}{3p}$ radians after $\vec{B}_B$. To create a rotating magnetic field in the air-gap, the three-phase winding is driven with three cosinusoidal currents, equally spaced apart in time:

$$i_A(t) = I_{pk}\cos(\omega_e t) \tag{2.24a}$$

$$i_B(t) = I_{pk}\cos\left(\omega_e t - \frac{2\pi}{3}\right) \tag{2.24b}$$

$$i_C(t) = I_{pk}\cos\left(\omega_e t + \frac{2\pi}{3}\right) \tag{2.24c}$$

where I_{pk} is the peak current through the winding, and ω_e is the electrical angular frequency, defined as the mechanical angular frequency multiplied by the number of pole-pairs, $\omega_e = p\omega_m$. Intuitively, $\vec{B}_A$ peaks at $t = 0$, $\vec{B}_B$ peaks at $t = \frac{2\pi}{3\omega_e}$, rotating the field by $\frac{2\pi}{3p}$ radians, $\vec{B}_C$ peaks at $t = \frac{4\pi}{3\omega_e}$, rotating the field by $\frac{2\pi}{3p}$ radians again, and the cycle repeats to create a rotating magnetic field.

As justified above, the three-phase stator winding is modeled as a surface current,

$$K_z(\phi, t) = K_{Az}(\phi, t) + K_{Bz}(\phi, t) + K_{Cz}(\phi, t). \tag{2.25}$$

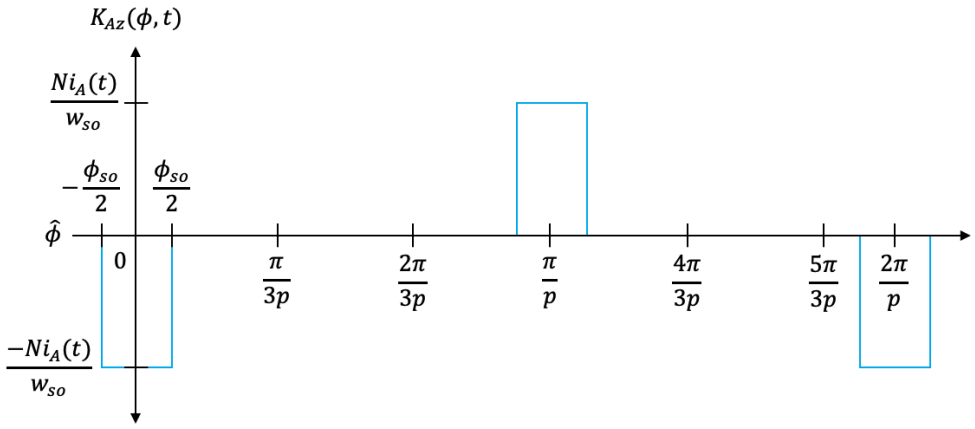

Figure 2.16: Surface current from the phase A winding over one spatial period

$K_{Az}(\phi, t)$ is the piece-wise continuous function depicted in Figure 2.16:

$$K_{Az}(\phi, t) = \begin{cases} -\frac{Ni_A(t)}{w_{so}} & -\frac{\phi_{so}}{2} \leq \phi \leq \frac{\phi_{so}}{2} \\ \frac{Ni_A(t)}{w_{so}} & \frac{\pi}{2p} - \frac{\phi_{so}}{2} \leq \phi \leq \frac{\pi}{2p} + \frac{\phi_{so}}{2} \end{cases} \tag{2.26}$$

where N is the number of turns per slot, w_{so} is width of the slot opening, and ϕ_{so} is the angular width of the slot opening given by

$$\phi_{so} = \frac{w_{so}}{R_s} \tag{2.27}$$

where R_s is the radius of the stator iron surface. Similarly,

$$K_{Bz}(\phi, t) = K_{Az}(\phi - \frac{2\pi}{3p}, t - \frac{2\pi}{3}) \tag{2.28a}$$

$$K_{Cz}(\phi, t) = K_{Az}(\phi + \frac{2\pi}{3p}, t + \frac{2\pi}{3}). \tag{2.28b}$$

The piece-wise continuous, periodic function $K_{Az}(\phi, t)$ can be represented as a Fourier series:

$$K_{Az}(\phi, t) = \sum_{n=1,3,5,\ldots}^{\infty} K_{an}(t) \cos(np\phi). \tag{2.29}$$

Only cosine functions are needed to represent $K_{az}(\phi,t)$ because it is an odd function, and only odd harmonics are necessary because $K_{az}(\phi,t)$ is halfwave anti-symmetric.

The Fourier coefficients $K_{An}(t)$ are given by the formula,

$$K_{an}(t) = \frac{2}{T}\int_{-\frac{T}{2}}^{\frac{T}{2}} K_{az}(t,\phi)\cos(np\phi)\,d\phi = \frac{4}{T}\int_{-\frac{T}{4}}^{\frac{T}{4}} K_{az}(t,\phi)\cos(np\phi)\,d\phi \tag{2.30a}$$

$$T = \frac{2\pi}{p} \tag{2.30b}$$

where T is the spatial period of $K_{az}(\phi,t)$, taking advantage of half-wave anti-symmetry. Substituting the definition of $K_{Az}(\phi,t)$ in Equation (2.26) into Equation (2.30a) results in

$$K_{An}(t) = -\frac{2p}{\pi}\int_{-\frac{\phi_{so}}{2}}^{\frac{\phi_{so}}{2}} \frac{Ni_a(t)}{w_{so}}\cos(np\phi)\,d\phi = -\frac{4}{n\pi w_{so}}\sin\left(np\frac{\phi_{so}}{2}\right) NI_{pk}\cos(\omega_e t). \tag{2.31a}$$

Abbreviating Equation (2.31a) gives

$$K_{An}(t) = K_n\cos(\omega_e t) \tag{2.31b}$$

where

$$K_n = -\frac{4NI_{pk}}{n\pi w_{so}}\sin\left(np\frac{\phi_{so}}{2}\right). \tag{2.31c}$$

Substituting the Fourier coefficients, Equation (2.31b), into Equation (2.29) gives

$$K_{Az}(\phi,t) = \sum_{n=1,3,5,\ldots}^{\infty} K_n\cos(\omega_e t)\cos(np\phi). \tag{2.32}$$

Applying the cosine addition formula,

$$\cos(\alpha+\beta) = \cos(\alpha)\cos(\beta) - \sin(\alpha)\sin(\beta), \tag{2.33}$$

to Equation (2.32) allows each harmonic of $K_{Az}(\phi,t)$ to be written as the sum of a forward

and backward travelling wave according to

$$K_{Az}(\phi,t)=\sum_{n=1,3,5,\ldots}^{\infty}\frac{K_n}{2}\Big[\cos(\omega_e t-np\phi)+\cos(\omega_e t+np\phi)\Big]. \tag{2.34a}$$

Similarly, $K_{Bz}(\phi,t)$ and $K_{Cz}(\phi,t)$ are given by rotating $K_{Az}(\phi,t)$ forward and backward $\frac{2\pi}{3p}$ in space and $\frac{2\pi}{3\omega_e}$ in time, respectively, resulting in

$$\begin{aligned}K_{Bz}(\phi,t)=\sum_{n=1,3,5,\ldots}^{\infty}\frac{K_n}{2}\Bigg[&\cos\left(\left(\omega_e t-\frac{2\pi}{3}\right)-np\left(\phi-\frac{2\pi}{3p}\right)\right)\\&+\cos\left(\left(\omega_e t-\frac{2\pi}{3}\right)+np\left(\phi-\frac{2\pi}{3p}\right)\right)\Bigg]\end{aligned} \tag{2.34b}$$

$$\begin{aligned}K_{Cz}(\phi,t)=\sum_{n=1,3,5,\ldots}^{\infty}\frac{K_n}{2}\Bigg[&\cos\left(\left(\omega_e t+\frac{2\pi}{3}\right)-np\left(\phi+\frac{2\pi}{3p}\right)\right)\\&+\cos\left(\left(\omega_e t+\frac{2\pi}{3}\right)+np\left(\phi+\frac{2\pi}{3p}\right)\right)\Bigg].\end{aligned} \tag{2.34c}$$

Summing all of the forward travelling components of $K_z(\phi,t)$ together gives

$$\begin{aligned}K_{z,forward}(\phi,t)=\sum_{n=1,3,5,\ldots}^{\infty}\frac{K_n}{2}\Bigg[&\cos\left(\omega_e t-np\phi\right)\\&+\cos\left(\omega_e t-np\phi-\frac{2\pi}{3}(n-1)\right)+\cos\left(\omega_e t-np\phi+\frac{2\pi}{3}(n-1)\right)\Bigg].\end{aligned} \tag{2.35}$$

The three components of $K_{z,forward}(\phi,t)$ are in phase if $n-1$ is a multiple of 3,

$$n=3k+1,\qquad k\in Z^{+}, \tag{2.36}$$

otherwise, they form a balanced three phase set and sum to zero. Therefore, $K_{z,forward}(\phi,t)$

can be written as

$$K_{z,forward}(\phi,t) = \sum_{n=1,7,13,\ldots}^{\infty} \frac{3K_n}{2}\cos(\omega_e t - np\phi) \tag{2.37}$$

where the even harmonics are excluded because $K_{z,forward}(\phi,t)$ is odd.

Summing all of the backward travelling components of $K_z(\phi,t)$ together gives

$$K_{z,backward}(\phi,t) = \sum_{n=1,3,5,\ldots}^{\infty} \frac{K_n}{2}\Bigg[\cos\left(\omega_e t + np\phi\right) + \cos\left(\omega_e t + np\phi - \frac{2\pi}{3}(n+1)\right) + \cos\left(\omega_e t + np\phi + \frac{2\pi}{3}(n+1)\right)\Bigg]. \tag{2.38}$$

The three components of $K_{z,backward}(\phi,t)$ are in phase if $n+1$ is a multiple of 3,

$$n = 3k-1, \quad k \in Z^+, \tag{2.39}$$

otherwise, they form a balanced three phase set and sum to zero. Therefore, $K_{z,backward}(\phi,t)$ can be written as

$$K_{z,backward}(\phi,t) = \sum_{n=5,11,19\ldots}^{\infty} \frac{3K_n}{2}\cos(\omega_e t + np\phi) \tag{2.40}$$

where the even harmonics are excluded because $K_{z,backward}(\phi,t)$ is odd.

Adding $K_{z,forward}(\phi,t)$ and $K_{z,backward}(\phi,t)$ together gives the total surface current density:

$$K_z(\phi,t) = \sum_{n=1,7,13,\ldots}^{\infty} \frac{3K_n}{2}\cos(\omega_e t - np\phi) + \sum_{n=5,11,19\ldots}^{\infty} \frac{3K_n}{2}\cos(\omega_e t + np\phi). \tag{2.41}$$

The surface current expressed in Equation (2.41) is used, along with the Halbach array rotor field from Section 2.2, to calculate the torque produced by a machine with a slotted stator and a Halbach array rotor in Section 2.3.2.

2.3.2 Torque Calculation

The torque produced by a machine with a Halbach array rotor, with air-gap fields given in Section 2.2, and a slotted stator, modeled as a smooth iron cylinder with a surface current given by Equation (2.41), is calculated using the Lorentz-Kelvin force density, given by

$$F_{LK} = \vec{J}_f \times \mu_0 \vec{H} + \mu_0 \vec{M} \cdot \nabla \vec{H}. \tag{2.42}$$

This force density describes the force per unit volume in a magneto-quasistatic system. Integrating F_{LK} over the stator gives the total shear force experienced by the stator as

$$f_\phi(t) = L \int_0^{2\pi} K_z(\phi, t) \mu_0 H_r(R_s, \phi, t)\, R_s d\phi \tag{2.43}$$

where L is the active length of the machine, $K_z(\phi, t)$ is defined in Equation (2.41), and H_r is the radial directed component of the magnetic field at the surface of the stator, R_s. Because the stator alone will not produce a shear force on itself, H_r in Equation (2.43) only needs to include the magnetic field caused by the rotor. The radial component of the rotor field is given in Equation (2.22) and is repeated here, evaluated at $r = R_s$, in the abbreviated form

$$H_r(R_s, \phi') = \sum_{n=1}^{\infty} H_{rn}(R_s) \cos(np\phi') \tag{2.44}$$

where the coefficient $H_{rn}(R_s)$ is found by evaluating Equation (2.22) at $r = R_s$, and ϕ' is the tangential axis of the rotating reference frame, defined with respect to the tangential axis of the stationary reference frame as

$$\phi' = \phi - \frac{\omega_e t}{p}. \tag{2.45}$$

ϕ' could be shifted by an additional constant phase shift, but with Equation (2.41) and Equation (2.44), the stator and rotor fields are $\frac{\pi}{2p}$ apart, resulting in maximum torque, so the additional phase shift is omitted.

The stator surface current in Equation (2.41) transformed to the rotating reference frame is given by

$$K_z(\phi', t) = \sum_{n=1,7,13,\ldots}^{\infty} \frac{3K_n}{2} \cos\left(np\phi' + \omega_e t(n-1)\right) + \sum_{n=5,11,19\ldots}^{\infty} \frac{3K_n}{2} \cos\left(np\phi' + \omega_e t(n+1)\right). \quad (2.46)$$

The shear force on the stator, Equation (2.43), evaluated in the rotating reference frame is given by

$$f_\phi(t) = \mu_0 L R_s \int_0^{2\pi} K_z(\phi', t) H_r(R_s, \phi')\, d\phi'. \quad (2.47a)$$

Substituting $K_z(\phi', t)$ from Equation (2.46) and $H_r(R_s, \phi')$ from Equation (2.44) results in

$$f_\phi(t) = \frac{3}{2}\pi\mu_0 L R_s \left[\sum_{n=1,7,13,\ldots}^{\infty} K_n H_{rn}(R_s) \cos(\omega_e t(n-1)) + \sum_{n=5,11,19,\ldots}^{\infty} K_n H_{rn}(R_s) \cos(\omega_e t(n+1)) \right]. \quad (2.47b)$$

The coefficients K_n are negative, whereas the rest of the constants in Equation (2.47b) are positive, so the shear force pulls the stator field against the direction of motion, $\hat{\phi}$. Intuitively, the stator field, which is $\frac{\pi}{2p}$ ahead of the rotor field, is pulled backward because the fields want to align with each other.

Torque is defined as the cross product of lever arm and force;

$$T = l \times f. \quad (2.48)$$

Substituting the shear force on the stator given in Equation (2.47b) into Equation (2.48) gives the torque on the stator. The torque on the rotor is equal to the opposite of the torque

on the stator. The torque on the rotor is given by

$$T = -\frac{3}{2}\pi\mu_0 L R_s^2 \left[\sum_{n=1,7,13,\ldots}^{\infty} K_n H_{rn}(R_s) \cos(\omega_e t(n-1)) + \sum_{n=5,11,19,\ldots}^{\infty} K_n H_{rn}(R_s) \cos(\omega_e t(n+1)) \right] \hat{z}. \quad (2.49)$$

Equation (2.49) reveals that the fundamental components of the radial rotor field and the stator surface current create a constant, average torque, and the higher harmonics are responsible for torque ripple.

2.3.3 Model Validation

The expression for torque in Equation (2.49) matches the torque calculated numerically with FEA to within 1.2% for an outer rotor machine, as seen in Figure 2.17. The FEA calculated torque in Figure 2.17 was obtained using the slotted stator geometry in Figure 2.18c, the mesh in Figure 2.20a, and linear steel.

The torque produced by the ideal stator geometry shown in Figure 2.18b, with smooth circular stator iron and surface currents, calculated with FEA, matches the torque produced by the practical stator with deep slot sections, shown in Figure 2.18c, calculated with FEA to within 0.1%, as seen in Figure 2.18a. This demonstrates that the slotted stator can be accurately modeled as a smooth circular iron supporting a surface current.

The torque produced by the practical stator geometry, shown in Figure 2.18c, calculated using FEA with the realistic, saturation-prone stator iron, Vacoflux 48, matches the torque produced with linear steel to within 0.1%, as seen in Figure 2.19. The vector plot in Figure 2.18c shows that the flux density in the stator iron is below the 2.3 T saturation limit for Vacoflux 48 [12]. This demonstrates that the stator iron can be accurately modeled as infinitely permeable, as is done in Section 2.2, when the iron does not saturate.

The torque produced by the practical stator geometry, shown in Figure 2.18c, calculated

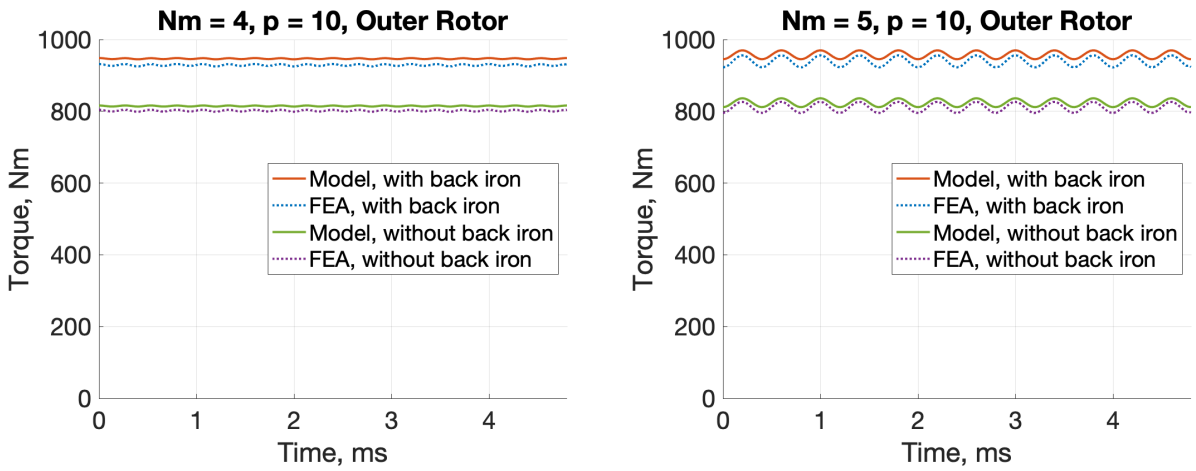

(a) (b)

Figure 2.17: Torque calculated with model matches FEA to within 1.2% over one electrical period for an outer rotor, ten-pole-pair Halbach array machine with four and five of segments per pole ($R_1 = 128.5$ mm, $R_2 = 131.5$ mm, $R_3 = 141.8$ mm, $I_{peak} = 1040$ A, $w_{so} = 2.5$ mm, $B_r = 1.19$ T, $\omega_e = 13087$ rad/s).

with 3D FEA, using the mesh in Figure 2.20b and Figure 2.20c, matches the torque calculated with 2D FEA, using the mesh in Figure 2.20a, within 0.1%, as shown in Figure 2.21. 3D FEA produces more accurate results than 2D FEA by modeling 3D effects such as eddy currents. Because 3D and 2D match to within 0.1%, 2D FEA was used to test the model throughout this chapter to save calculation time and memory.

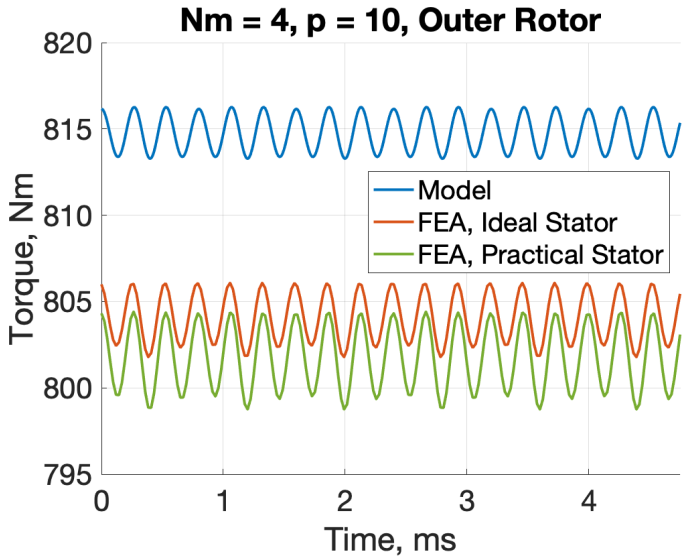

(a)

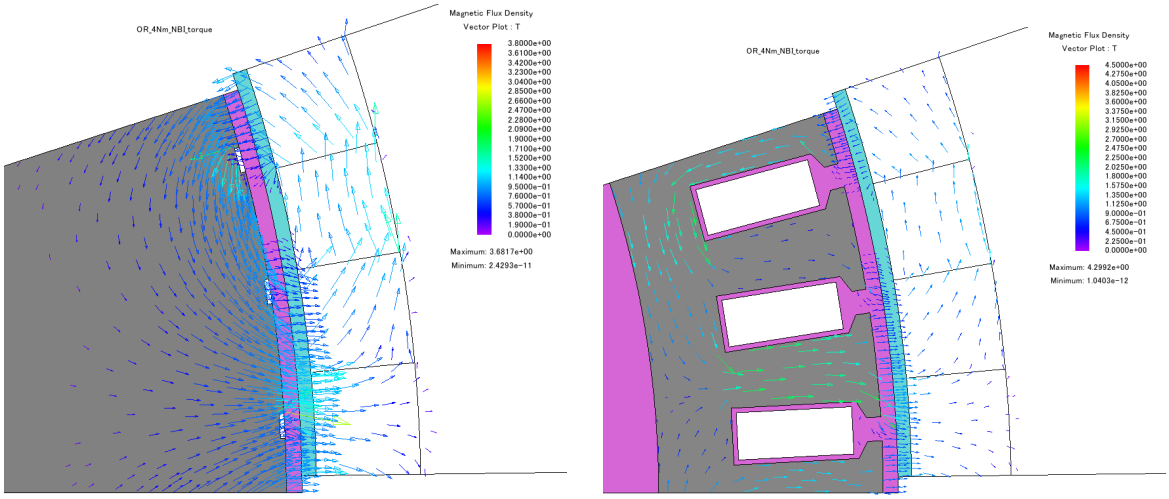

(b) (c)

Figure 2.18: Torque found with model matches FEA to within 1% for (b) ideal stator and (c) practical stator (Outer rotor, ten pole-pair, $N_m = 4$, $R_1 = 128.5$ mm, $R_2 = 131.5$ mm, $R_3 = 141.8$ mm, $I_{peak} = 1040$ A, $w_{so} = 2.5$ mm, $B_r = 1.19$ T, $\omega_e = 13087$ rad/s).

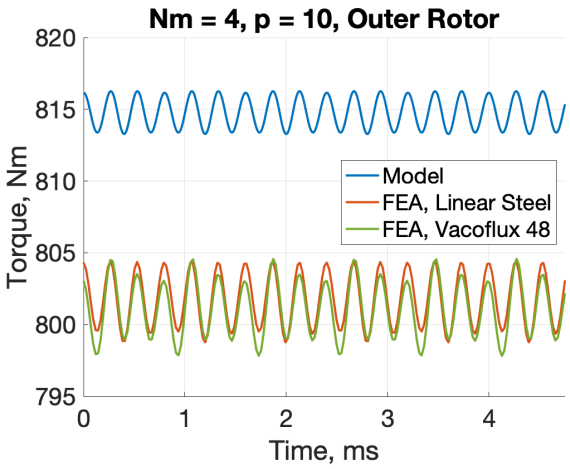

Figure 2.19: Torque found with model matches FEA to within 1% for practical stator with realistic stator steel (Vacoflux 48) and linear steel (Outer rotor, ten-pole-pair, $N_m = 4$, $R_1 = 128.5$ mm, $R_2 = 131.5$ mm, $R_3 = 141.8$ mm, $I_{peak} = 1040$ A, $w_{so} = 2.5$ mm, $B_r = 1.19$ T, $\omega_e = 13087$ rad/s).

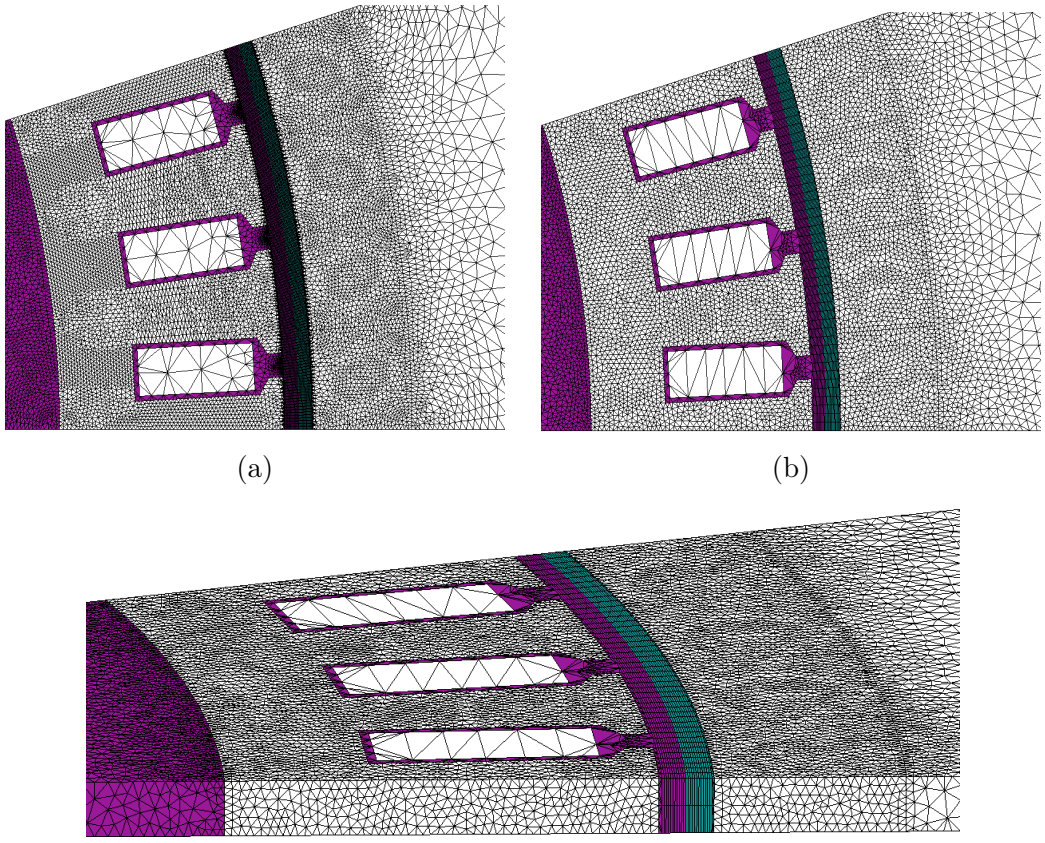

(a) (b)

(c)

Figure 2.20: (a) Mesh used for 2D FEA (b) Mesh used for 3D FEA, top view (c) Mesh used for 3D FEA, side view.

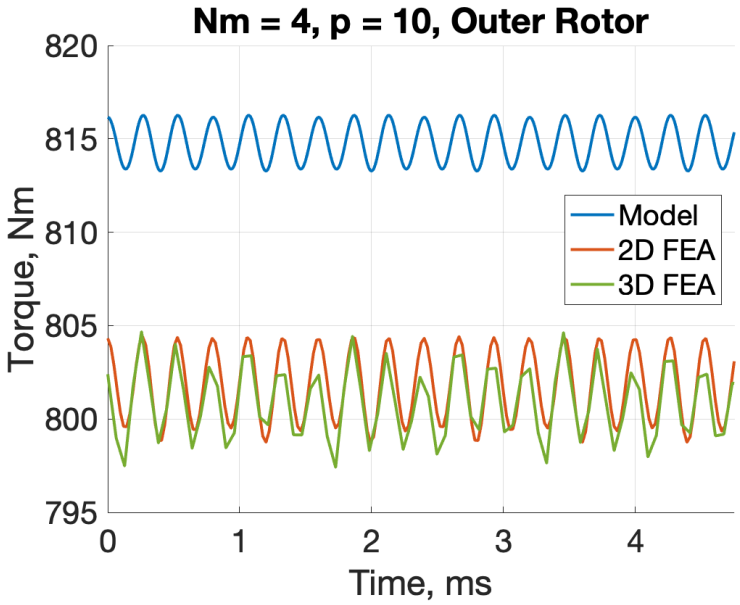

Figure 2.21: Torque found with model matches 2D FEA and 3D FEA to within 1% for practical stator (Outer rotor, ten-pole-pair, $N_m = 4$, $R_1 = 128.5$ mm, $R_2 = 131.5$ mm, $R_3 = 141.8$ mm, $I_{peak} = 1040$ A, $w_{so} = 2.5$ mm, $B_r = 1.19$ T, $\omega_e = 13087$ rad/s).

	Model	2D FEA	3D FEA
Computation time [s]	$5.6 * 10^{-4}$	44	820

Table 2.1: Torque calculation time for model, 2D FEA, and 3D FEA.

2.4 Discussion

As illustrated in Table 2.1, the torque in Equation (2.49) was calculated using the MATLAB function in Appendix A in 1/100,000 of the time that it took to calculate with 2D FEA, with 200 time steps per electrical period, and in 1/1,500,000 of the time that it took to calculate with 3D FEA, with 75 time steps per electrical period. Although the calculation time for FEA could be decreased by using a mesh with larger elements than those in 2.20 and fewer time steps, calculating the torque using Equation (2.49) will always be several orders of magnitude faster than using FEA.

Due to the advantage in computational time, the torque calculation in Section 2.3.3 is

recommended for sweeping parameters like machine radii, number of magnet segments of per pole, etc, in the initial design of a Halbach array rotor, slotted stator electric machine. Once an initial design candidate is found which satisfies all constraints and maximizes performance, FEA is recommended for the detailed design of the parameters which were simplified in this model, such as stator slot section geometry, stator back iron width, and rotor back iron width. Figure 2.17 shows that a practical machine design, shown in Figure 2.18c, can achieve the torque calculated by the idealized model within 1.2%. The machine shown in Figure 2.18c is currently in manufacture, with testing planned this year.

Additionally, the models presented in this chapter are useful for describing how, and explaining why, individual parameters of the electric machine affect the torque. For example, the number of magnet segments per pole in the Halbach array rotor, N_m, is varied for an outer rotor, ten-pole-pair machine, while all other parameters are held constant, and the torque, calculated using Equation (2.49), is plotted over one electrical period in Figure 2.22. Generally, the average torque produced by the machine increases and the torque ripple decreases as the number of segments increases. However, the torque ripple increases when increasing N_m from 1 to 2 and from 4 to 5, and the average torque decreases when increasing N_m from 1 to 2 when rotor back iron is included, as seen in Figure 2.22.

Intuitively, increasing N_m, which increases the sampling frequency of the ideal rotating magnetization density and thus decreases the harmonic distortion of $\vec{M}$, should lead to less torque ripple and higher average torque. Therefore, one might suspect an error with the numerical simulation setup if only given the results obtained with FEA in Figure 2.17. However, the torque in Equation (2.49) shows that every harmonic of the Halbach array rotor field does not contribute equally to torque ripple. Instead, torque ripple is produced at a certain harmonic only when both radial rotor field and stator surface are nonzero. Comparing the harmonics of the radial rotor field in Figure 2.23 to the harmonics of the concentrated-wound, three-phase stator surface current in Figure 2.23e explains why torque ripple increases as N_m increases from 1 to 2 and 4 to 5. Furthermore, comparing the first

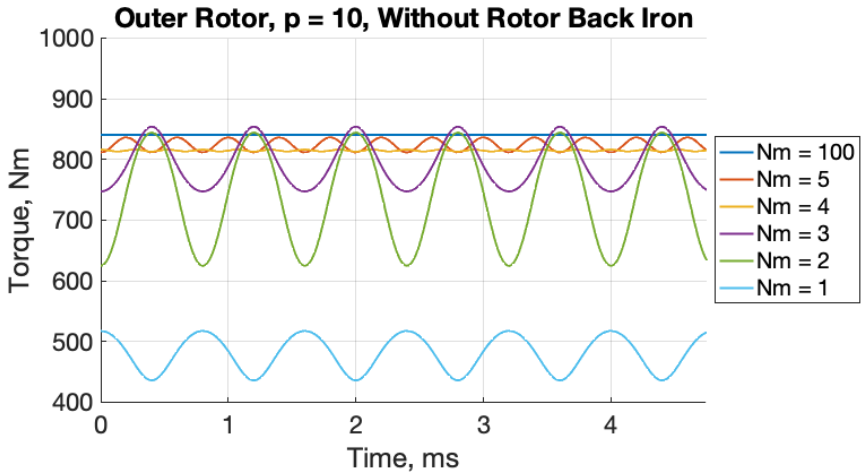

(a)

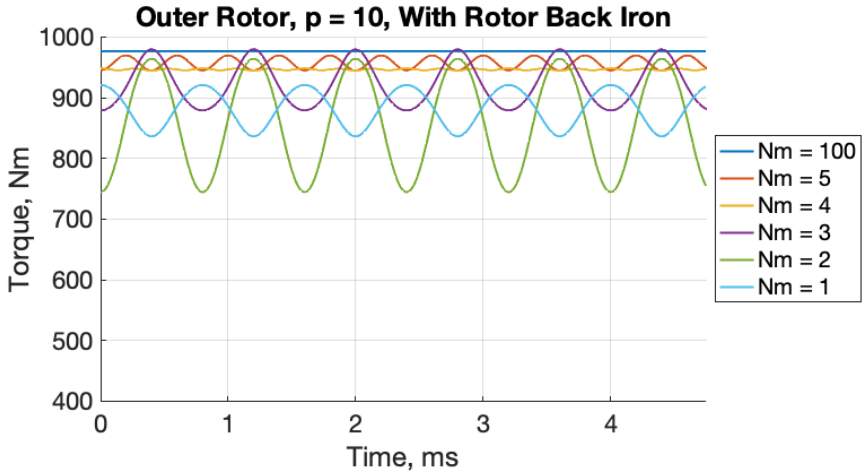

(b)

Figure 2.22: Torque produced by an outer rotor, 10 pole-pair Halbach array machine with an increasing number of segments per pole (a) without rotor back iron and (b) with rotor back iron.

harmonics of the radial rotor fields in Figure 2.23b explains why the average torque decreases as N_m increases from 1 to 2 when including rotor back iron.

A Halbach array rotor with four magnet segments per pole and no back iron was selected for use in the 1-MW demonstrator, as the optimal balance between performance and manufacturing complexity, based on the model described in this chapter and feedback from the rotor manufacturer. As seen in Figure 2.22, for an outer-rotor, ten-pole-pair Halbach array rotor machine with a concentrated-wound, three-phase, slotted stator, the relative increase

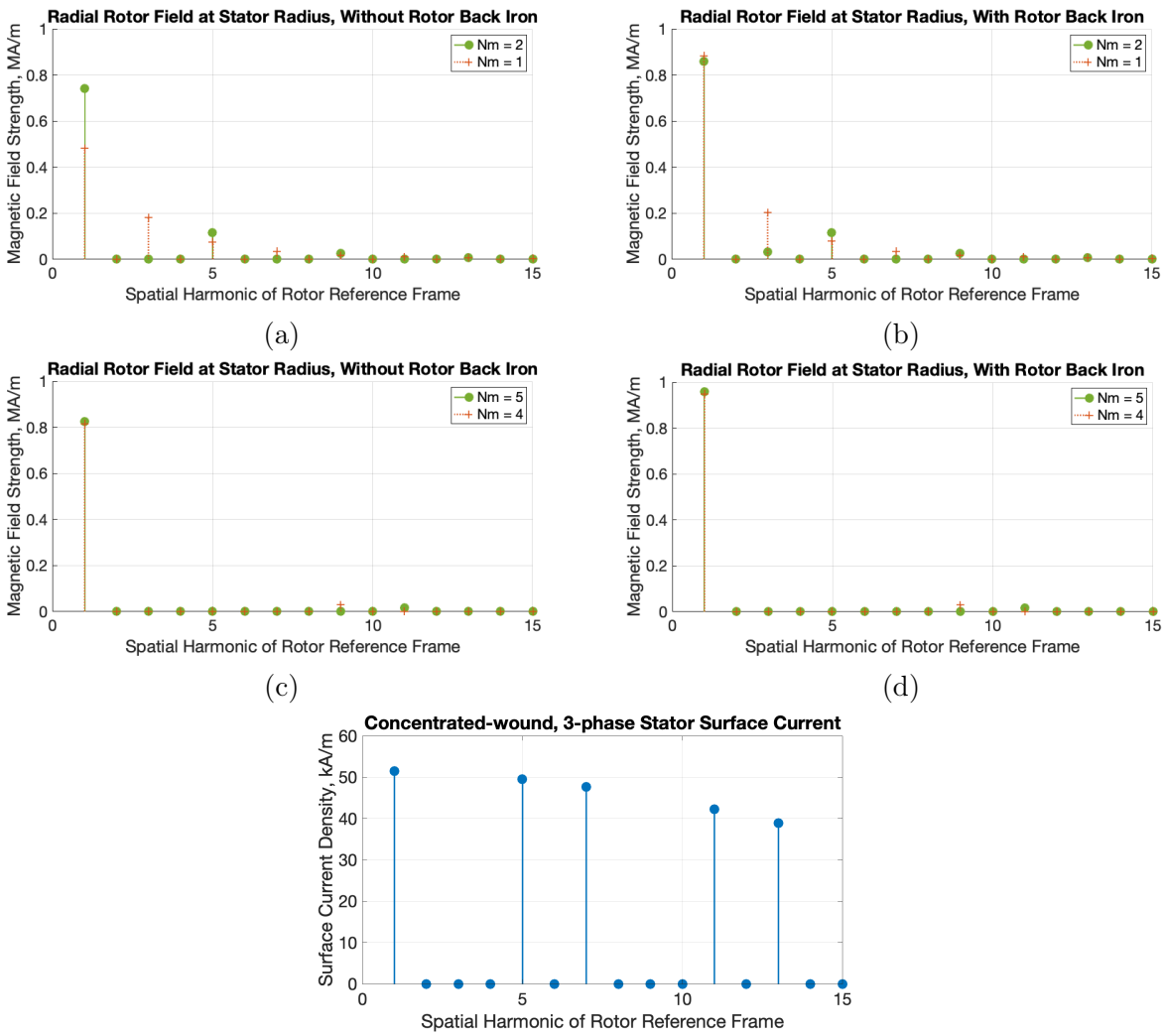

Figure 2.23: (a), (b), (c), (d) Harmonics of the radial Halbach array rotor field at the stator radius, $H_{rn}(R_s)$, and (e) Harmonics of concentrated-wound, three-phase stator surface current, K_n, explain why torque ripple increases as N_m increases from 1 to 2 and 4 to 5.

in average torque and decrease in torque ripple diminishes when increasing N_m above four. A titanium rim was used to retain the magnets instead of rotor back iron. The improved mechanical strength and reduced mass of the titanium rim outweighed the benefit of increased torque given from rotor back iron, as seen in Figure 2.22 [4].

In summary, the models described in this chapter can be used to calculate the torque of a machine with a Halbach array rotor and slotted stator 100,000 times faster than 2D FEA while remaining accurate to within 1.2% of 2D FEA, to describe how individual parame-

ters affect machine performance, and to explain counter-intuitive trends in machine torque. Therefore, these models are recommended for use in the initial design of other Halbach array rotor, slotted stator machines.

Although the models presented in this chapter are specific to machines with Halbach array rotors and slotted stator, the techniques behind these models,

- representing a stator winding as a surface current,
- representing a slotted stator as a smooth iron cylinder, and
- using Fourier series representations of piece-wise continuous functions to simplify equations,

can be used to construct analytical models for other types of electric machines.

Chapter 3

Characterizing the Effect of Stress on the Magnetic Properties of Iron-Cobalt

3.1 Introduction

In this chapter, samples of iron-cobalt stator material are experimentally characterized at various stages of the stator-core manufacturing process. The objective is to understand how the stress applied during the stator manufacturing process affects the magnetic performance of the stator material and the electric machine. The details of the experimental setup are described in Section 3.3. In Section 3.4, a conventional lamination bonding process is shown to increase core loss by 20% at the operating point of the 1-MW electric machine. Two manufacturing processes for iron-cobalt stators are compared in Section 3.5. In Section 3.6, the magnetic properties of a 0.5-inch tall stack of full-size stator laminations are measured. The partial stator measurements show good alignment with the smaller toroid samples used in Sections 3.4 and 3.5. Lastly, the implications of the effect of the manufacturing process on stator performance are discussed in Section 3.7.

3.2 Background

Grain-oriented iron-cobalt alloys, commonly referred to by the trade name Super-Permendur (Supermendur), are popular for high-performance applications because they offer the highest saturation flux density (2.4 T) and lowest core loss of any material available. However, due to the high levels of Cobalt in the alloy, the core loss and permeability are exceptionally susceptible to the mechanical stress applied [13].

The electric machine's ability to achieve the full rated power of 1-MW relies heavily on minimized stator core loss, as it is expected to be the dominant loss [4]. To attain the most accurate prediction for stator core loss, the magnetic properties of the iron-cobalt stator material were measured after each step in the manufacturing process.

3.3 Experiment Setup

The specific core loss and B-H curve data presented in Sections 3.4 and 3.5 are collected using 40-mm diameter toroid samples (see Figure 3.1). The samples are wound with 90 primary turns and 30 secondary turns. A sinusoidal voltage amplifier drives the primary winding. An oscilloscope measures the open-circuit voltage on the secondary winding and the current in the primary winding (see Figure 3.2). The voltage on the secondary winding is caused only by induction, because no current flows through the secondary winding.

The magnetic field strength (H), flux density (B), and specific core loss ($\frac{P_c}{m_c}$) are calculated using Ampere's law,

$$H = \frac{N_1 I_1}{l_c}, \tag{3.1}$$

Faraday's law,

$$B = \frac{1}{N_2 A_c} \int V_2(t)\, dt, \tag{3.2}$$

(a) (b)

Figure 3.1: (a) Toroid sample of iron-cobalt material (b) Toroid sample in 3-D printed case with winding.

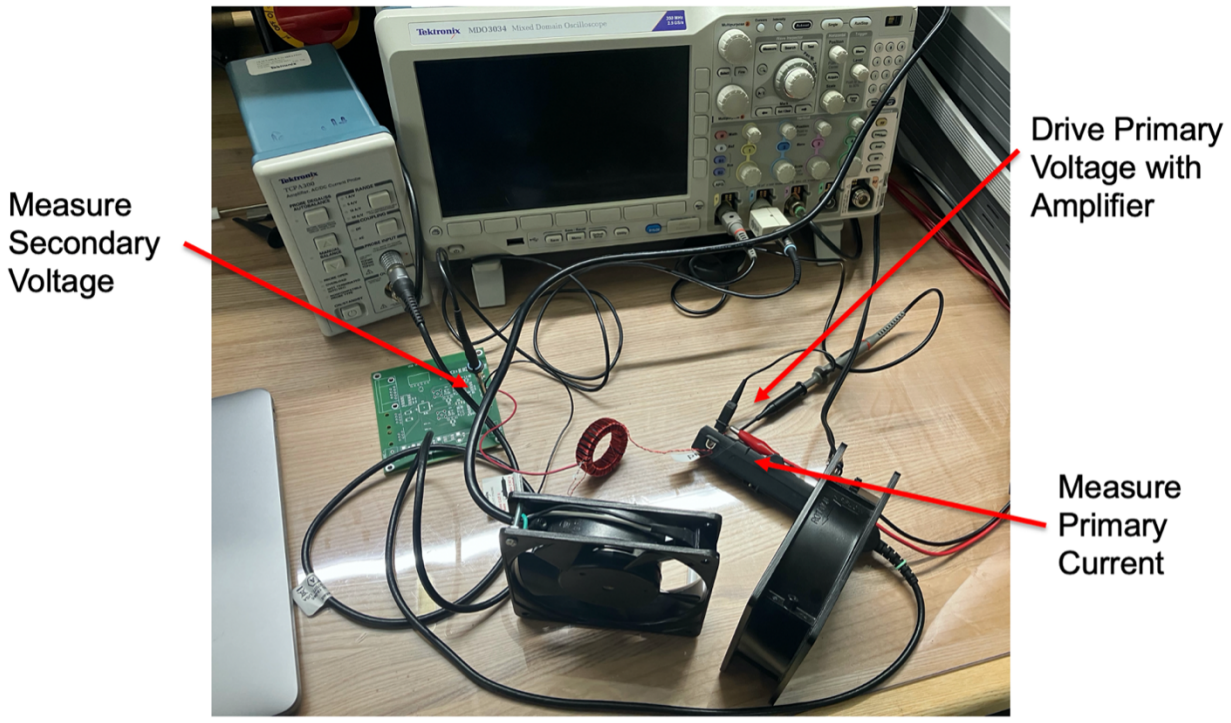

Figure 3.2: Experiment setup for characterizing soft-magnetic materials.

and integrating the electrical energy put into the system over a cycle,

$$\frac{P_c}{m_c} = \frac{1}{m_c T} \int_0^T I_1 \frac{N_1}{N_2} V_2(t)\, dt \tag{3.3}$$

where I_1 is primary current, V_2 is secondary voltage, N_1 and N_2 are number of primary and secondary turns respectively, A_c is cross sectional area of core, l_c is mean core length, m_c is mass of core, and T is period.

3.4 Effect of a Conventional Stator Lamination Bonding Process

The stator laminations for the 1-MW demonstrator were bonded together to facilitate winding the stator core. In a conventional lamination bonding process, an adhesive is applied to the individual laminations, the laminations are stacked on top of each other, and pressure (usually around 150 psi) is applied to the lamination stack while the adhesive cures [14].

To understand the impact of the bonding process on the magnetic properties of the iron-cobalt stator material, two samples of loose laminations and two samples of bonded laminations were experimentally characterized. The samples contained 32 toroid laminations each of 0.1-mm Vacoflux-48 material (49% Co, 49% Fe, 2% V).

As seen in Figure 3.3a, the bonding process significantly increased the core loss of the iron-cobalt stator material. Specifically, the bonding process increased the core loss of the stator material by 20% at the operating point of the electric machine stator (2.2 T, 2000 Hz).

Furthermore, the bonding process caused the B-H curve of the stator material to depreciate, as seen in Figure 3.3b. However, when the electric machine was simulated in FEA using the B-H curve from the bonded material, there was a negligible impact on performance. This is attributed to the fact that the machine operates near below the deep saturation regime

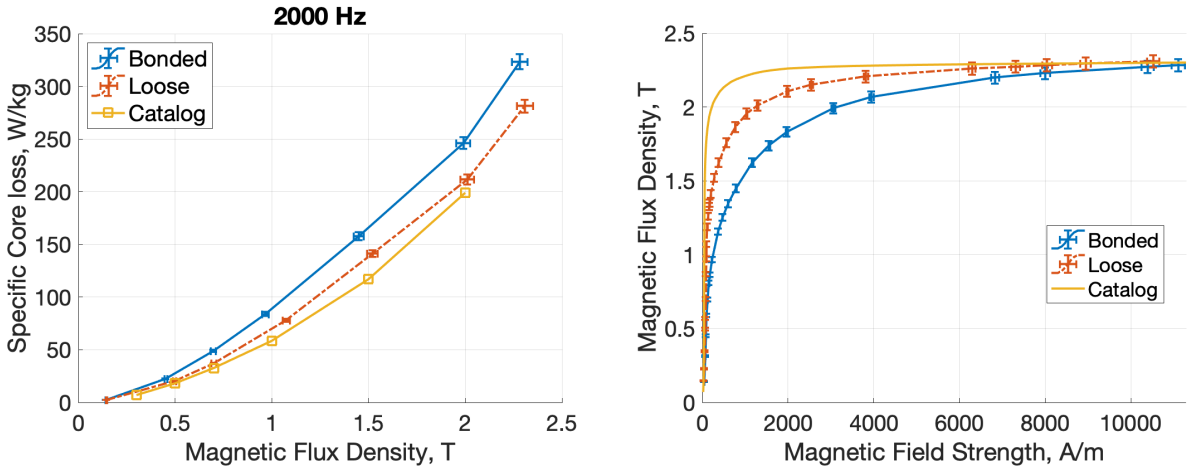

(a) Specific core loss at 2000 Hz

(b) Flux density as a function of field strength

Figure 3.3: Magnetic properties of 0.1 mm Vacoflux-48 (Fe-Co-V) laminations before and after bonding.

(>2.2 T) for both the B-H curves.

3.5 Comparing Stator Manufacturing Processes

An original stator manufacturing process was developed for the 1-MW demonstrator to minimize the stress on the laminations (referred to as Process #1, Figure 3.4). While pursuing the original process, an alternative stator manufacturing process became available under the product name "VACSTACK" (referred to as Process #2, Figure 3.4). Stator cores manufactured with both Process #1 and Process #2 were acquired (see Figure 3.5).

To determine which manufacturing process resulted in better magnetic performance, two toroid samples from both processes were experimentally characterized. The toroids from Process #1 did not undergo ID grinding. The results of the experimental characterization are shown in Figure 3.6.

The stator manufactured with Process #2 was only available with Vacodur 49, a variant of Vacoflux 48 with slightly lower magnetic performance and higher mechanical strength [12]. The specific core loss data provided by the manufacturer for Vacodur 49 is slightly higher than Vacoflux 48.

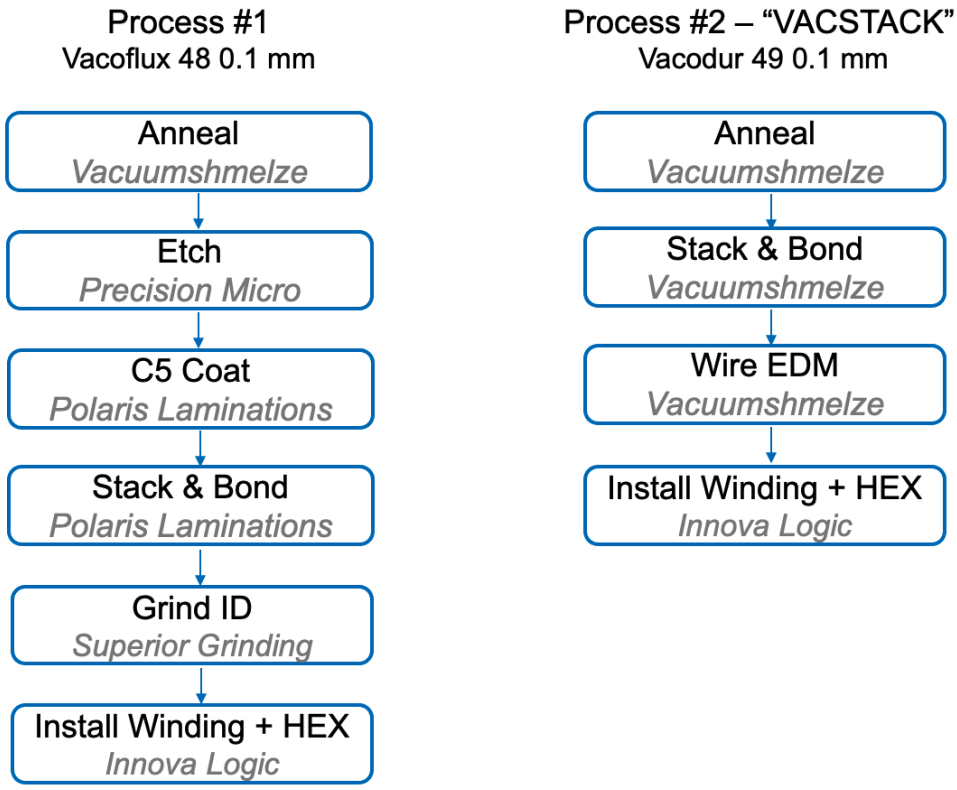

Figure 3.4: Two alternative manufacturing processes for stator cores.

As seen in Figure 3.6a, the specific core loss data measured on the samples from Process #1 are significantly higher than the catalog data for Vacoflux 48. In contrast, the specific core loss data measured on the samples from Process #2 closely match the catalog data for Vacodur 49. The catalog data for both alloys were measured on loose, unbonded laminations.

Similarly, the B-H curve measured on the samples from Process #2 is superior to that measured on the samples from Process #1, as shown in Figure 3.6b. When the electric machine was simulated with FEA using the B-H curve from Process #1, the torque was 1% lower and the peak flux density was 0.1 T lower than it was when simulated with the B-H curve from Process #2, as illustrated in Figure 3.7. The fact that the machine performance is similar with both B-H curves is attributed to the fact that the machine operates near below the deep saturation regime (>2.2 T) for both the B-H curves.

Manufacturing Process #2 is recommended for building future stators as it imparts less stress on the laminations and thus results in better magnetic performance.

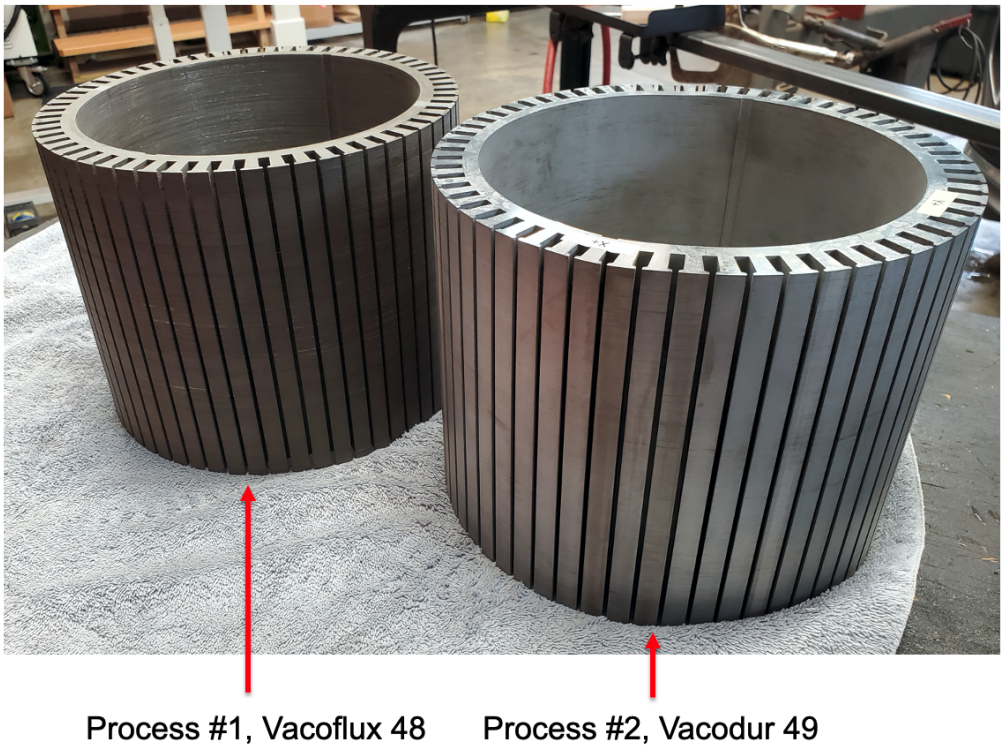

Figure 3.5: Two stator cores manufactured with different processes (courtesy of Marc Amato, Innova Logic LLC).

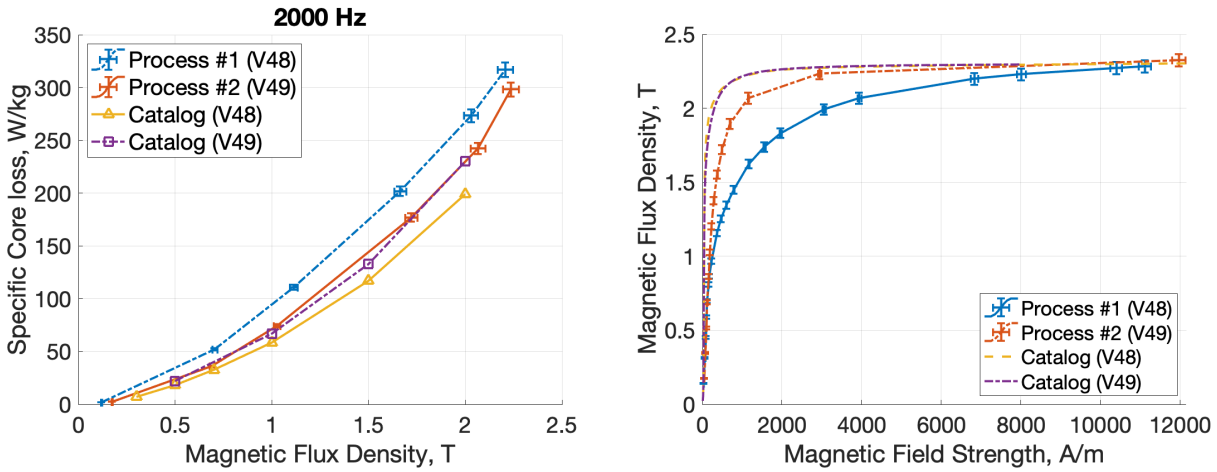

(a) Specific core loss at 2000 Hz

(b) Flux density as a function of field strength

Figure 3.6: Magnetic properties of Fe-Co-V alloys "Vacoflux 48" and "Vacodur 49" with different manufacturing processes.

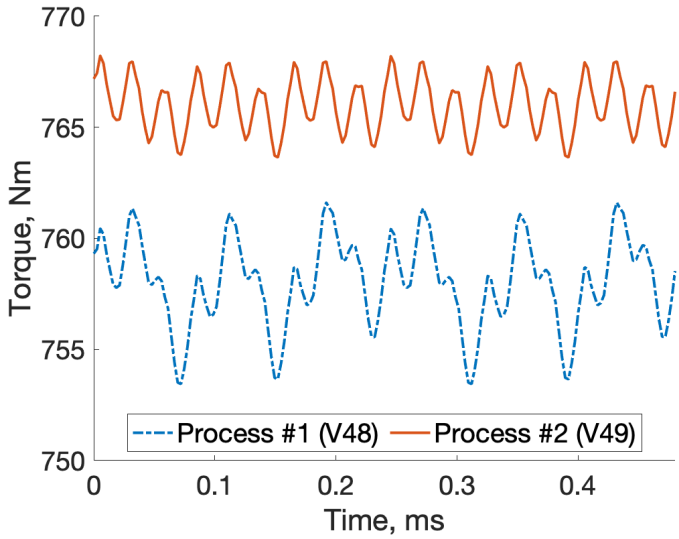

Figure 3.7: Torque of the machine via FEA using experimental data from different manufacturing processes.

3.6 Partial Stator Experiment

To verify that the data collected on the toroid samples in the Sections 3.4 and 3.5 accurately represents the electric machine, the magnetic properties of full-size stator laminations were measured. However, amplifiers capable of supplying enough power to drive the entire stator core were unavailable because they too were under development. Instead, specific core loss data from a 0.5-inch tall stack of bonded stator laminations, shown in Figure 3.8, were collected.

When the partial stator stack is wound in the same fashion as the toroid samples, as shown in 3.8b, the magnetic flux travels only through the back iron, since it offers the lowest reluctance path. This approximation was validated by simulating the partial stator stack with FEA, as shown in Figure 3.9. Therefore, the stator teeth can be ignored when analyzing the data presented here.

When measuring the core loss of the partial stator stack at 2,000 Hz (the electrical frequency of the machine), a natural frequency of the shortened stator shape was excited.

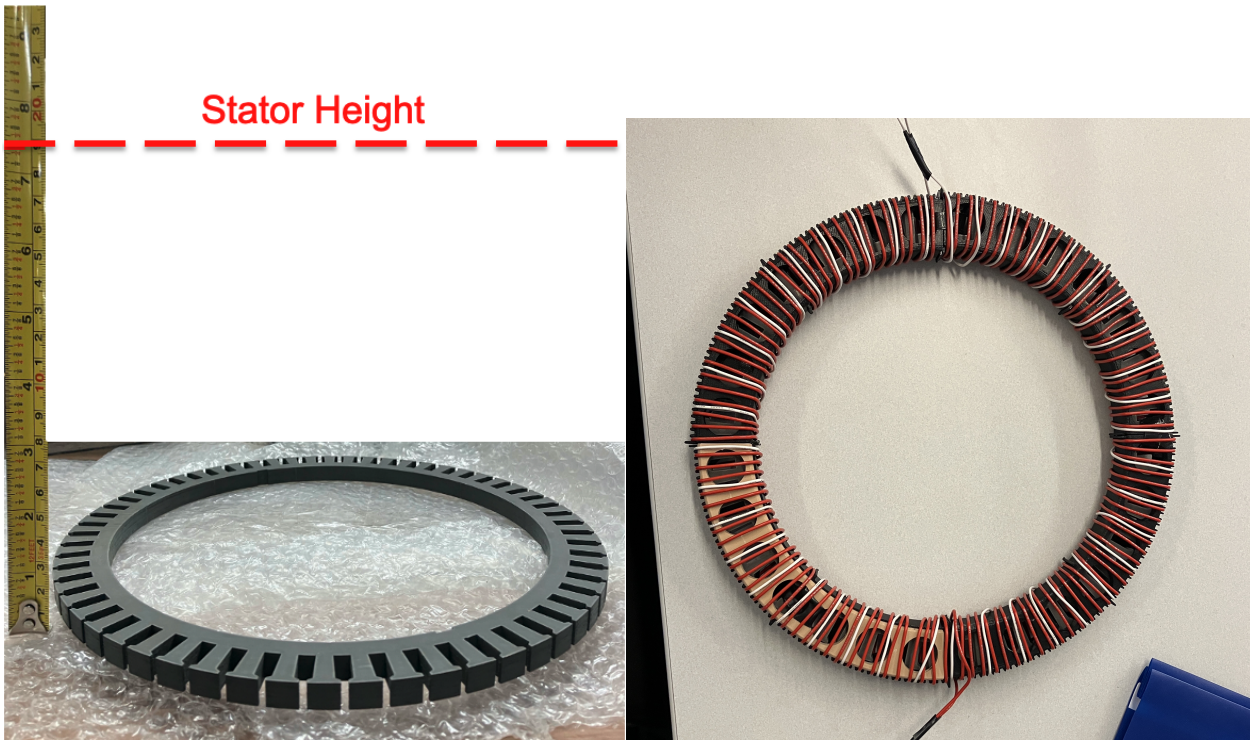

(a) (b)

Figure 3.8: (a) Partial stator stack (b) Partial stator stack in plastic case with winding.

The mechanical resonance caused excessive vibration, leading to higher than expected core loss measurements. When vibrating, magnetic energy is converted into mechanical energy and motion, and therefore the core-loss calculated by Equation (3.3), which assumes that all of the electrical energy input into the system is dissipated in core loss, is inaccurate. To avoid the natural frequency, the core loss of the partial stator was measured at 2,500 Hz.

As shown in Figure 3.10, the specific core loss measured on the partial stator stack closely matches that measured on the toroid samples. Therefore, the data from the toroid samples provides an accurate estimate for the full-size stator.

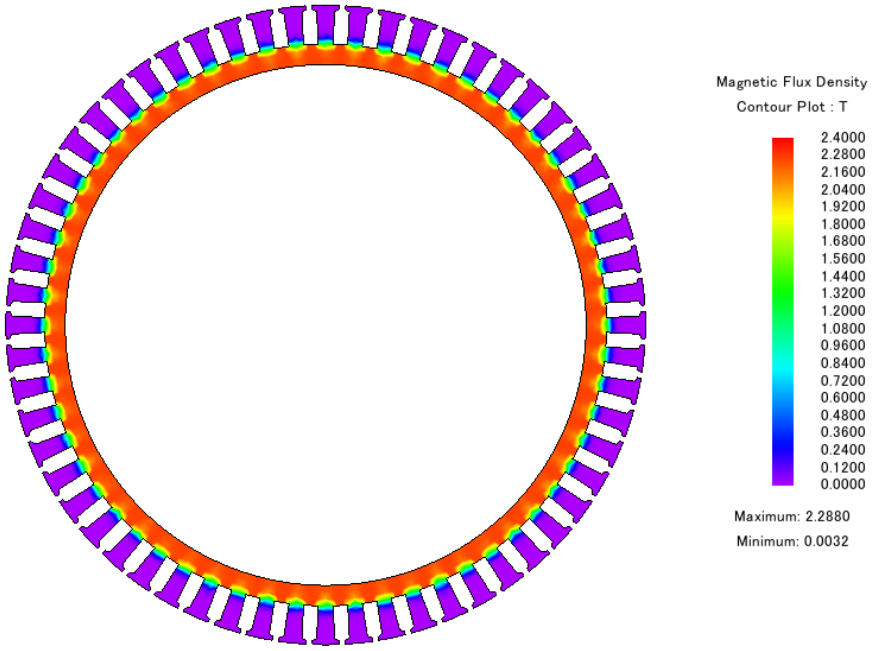

Figure 3.9: Flux density in partial stator experiment via FEA.

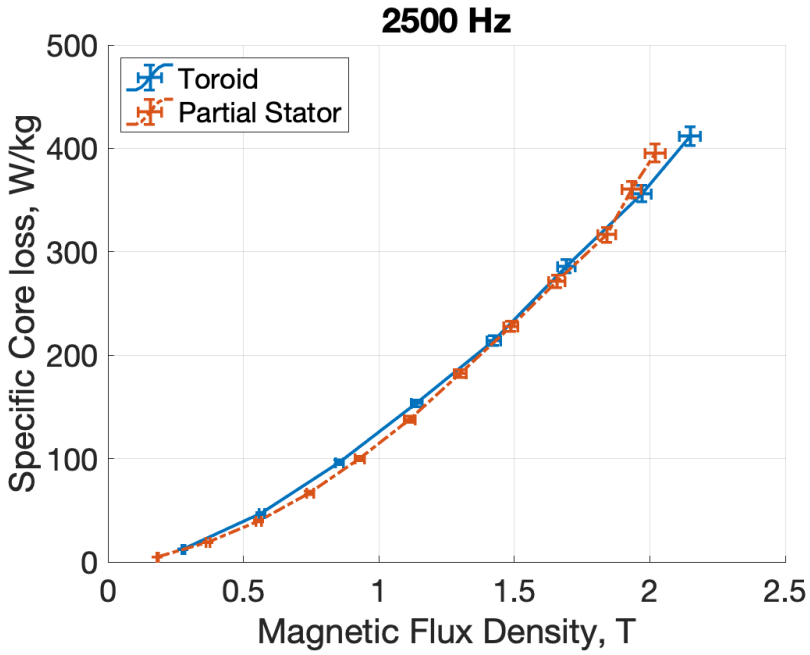

Figure 3.10: Specific core loss of the 200-mm-diameter partial stator matches that of the 40-mm-diameter toroid.

3.7 Discussion

Mitigating stator core loss is critical for building electric machines for aircraft propulsion, as achieving high specific power requires operating at high rotational speeds and electrical frequencies. As shown in Sections 3.4 and 3.5, the catalog core loss data can vary significantly from the actual stator core loss due to stress applied during the manufacturing process.

In the design of the electric machine, a safety factor of two was applied to the stator core loss estimate, which used "Vacoflux 48" catalog data measured on loose laminations. Including the safety factor lowered the rotational speed of the optimized machine by 20% [4]. The data shown in Sections 3.4 and 3.5 suggest that the stator core loss of the actual machine may be only 20% higher than the loose-lamination, "Vacoflux 48" catalog data. Therefore, the electric machine may be able to achieve higher rotational speeds and electrical frequencies within the thermal limit of the test setup.

However, other factors such as the effect of rotating magnetic fields and the stator to heat-sink interference fit may raise the stator core loss beyond what was measured in this chapter [15], [16]. The core loss measured on the 1-MW demonstrator, when available, should be used to recommend a new safety factor to apply to the catalag core loss data for iron-cobalt stator-cores manufactured with each of the two processes documented in Section 3.5.

For the design of future electric machines, obtaining measurements of the stator core material under the same stress as the actual stator is recommended to ensure the most accurate core loss estimate. If core loss data for the material under similar stress is not attainable, applying a safety factor to the catalog data measured on loose laminations is essential.

Chapter 4

Summary, Conclusion, and Suggestions for Future Work

4.1 Summary

In Chapter 2, the magnetic field produced by a cylindrical, segmented Halbach array was derived from Maxwell's Equations using the Fourier series representation of the magnetization density. A technique for modeling a slotted stator as a smooth iron cylinder with a surface current was applied to the concentrated-wound, three-phase stator used in the 1-MW demonstrator, and the torque was calculated using the Lorentz-Kelvin force density. The torque equation matches FEA to within 1.2% and computes 100,000 faster than 2D FEA, making it ideal for the initial machine design.

In Chapter 3, the stator core loss produced by the iron-cobalt laminations used in the 1-MW demonstrator was characterized using 1.5-inch diameter toroid samples and full-size, 10-inch diameter stator laminations. A conventional lamination bonding process was found to increase the core loss by 20% over loose, unbonded laminations. An alternative stator-core manufacturing process which results in no impact on core loss was identified and experimentally verified.

4.2 Conclusion

The model for the torque produced by a machine with a Halbach array rotor and slotted stator in Chapter 2 is recommend for the initial design of future machines. The reduced computation time of this model allows parameters, such as the number of segments in the Halbach array, the stator/rotor radii, and the stator current strength, to be swept in a fraction of the time that it would take using 2D FEA. Once an initial machine design is obtained, FEA is recommend for designing the parameters that were simplified in the models in Chapter 2, such as the stator slot geometry, the width of the stator back iron, and the width of the rotor back iron. The torque produced by the 1-MW demonstrator, calculated with FEA, matches the torque calculated with the simplified model within 1.2%.

Additionally, the models in Chapter 2 are useful for describing how, and explaining why, individual parameters of the machine affect performance. For example, the model was used to explain why increasing the number of magnet segments in a Halbach array machine can actually cause the torque ripple to increase.

Torque ripple is caused by the interaction of the harmonics of the stator field with the rotor field. Although increasing the number of magnet segments causes the harmonic distortion of the rotor field to decrease, it can also cause a harmonic of the rotor field to begin interacting with the stator field, leading to higher torque ripple.

For the concentrated-wound, three-phase stator in the 1-MW demonstrator, a Halbach array with four magnet segments per pole results in low torque ripple and high average torque while remaining within the manufacturing ability of the magnet vendor. Increasing the number of magnets segments per pole beyond four does not decrease the torque ripple by much, if it does at all. However, for machines with a different stator winding, the optimal number of magnet segments per pole may be very different.

The first attempt at analyzing the air-gap field produced by a cylindrical Halbach array for this thesis involved adapting a technique previously used to analyze linear Halbach arrays.

The tangential magnetization density was replaced with free surface currents, and the scalar potential in the magnet region satisfied Laplace's Equation. This method led to a 10% error between the model and FEA. Although this technique works for linear arrays, for cylindrical arrays, $\nabla \cdot \vec{M} \neq 0$ in the magnet region, even when the tangential component is replaced with surface currents. Therefore, the scalar potential in the magnet region must satisfy Poisson's Equation instead of Laplace's Equation. When the scalar potential in the magnet region satisfies Poisson's Equation, the model matches FEA to within 1%. This illustrates that models for linear machines do not always apply for cylindrical machines.

Although the models presented in Chapter 2 are specific to machines with Halbach array rotors and slotted stator, the techniques behind these models,

- representing a stator winding as a surface current,
- representing a slotted stator as a smooth iron cylinder, and
- using Fourier series representations of piece-wise continuous functions to simplify equations,

can be used to construct analytical models for other types of electric machines.

The experimental results in Chapter 3 demonstrate that the core loss of iron-cobalt laminations can rise by as much as 20% depending on the stress applied during the manufacturing process. However, when the stator-core was manufactured by one company from start to finish, there was no observed rise in core loss. Therefore, reducing the number of steps and companies involved in the stator manufacturing process is recommended to reduce stator core loss. Otherwise, a safety factor should be applied to the catalog core loss data to account for the stress of the manufacturing process.

The core loss measured on a stack of full-size, slotted stator laminations was found to match the core loss measured on a smaller, smooth, toroid sample within the error of the experiment in Chapter 3. This demonstrates that stator core loss can be accurately measured using the real stator, even if it has slots, if toroid samples are not available. On the other

hand, if the real stator cannot be measured directly, then measuring toroid samples should result in an accurate core loss estimate.

4.3 Suggestions for Future Work

The 1-MW demonstrator is planned for full power testing in 2024. The torque produced by the real machine should be compared with the torque calculated in Chapter 2 and FEA to gauge how accurately the model predicts the torque produced by real electric machinery. Given that the fields on the real rotor match the model to within the 5% error of the experimental setup, the average torque should also match the model to within around 5%, and the torque ripple should not exceed more than 2% of the average torque.

The equation for the rotor fields in Chapter 2, Equation (2.22), results in infinity for machines with a single pole-pair, $p = 1$. The model can be extended to apply for machines with a one pole-pair by starting the equations in Section 2.2 with $p = 1$ and avoiding division by zero.

As the slot width goes to zero, the surface current becomes infinitely large, while the area that it is integrated over goes to zero. Ideally, these two extremes counteract each other, and the torque does not go to infinity. However, the Fourier series used to represent the stator surface current cannot accurately represent the impulse function, so the torque calculated in Chapter 2 goes to infinity as the slot width goes to zero. The torque expression in Chapter 2 could be compared with FEA over a range of different slot widths to determine at what point the model is no longer accurate.

In Chapter 3, the stress applied during a conventional lamination bonding process was found to increase the core loss of the iron-cobalt laminations by 20%. The interference fit between the heat sink and the stator core may also apply significant stress to the laminations. The core loss of the 1-MW demonstrator can be separated from the other losses during testing, and used to estimate the impact of the interference fit on core loss. Furthermore,

the core loss of the 1-MW demonstrator can be used to recommend a general safety factor to apply to catalog core loss data for iron-cobalt laminations.

Appendix A

MATLAB Code listing

Function for calculating α_n ("M_r_n_cos") and β_n ("M_phi_n_sin") using equation (2.9d) and equation (2.10):

```
function [M_r_n_cos, M_phi_n_sin] = get_mag_FS_coeffs(N_m,
   inner_rotor, M_o, p, num_harmonics)
    del_phi = pi/(p*N_m);   % angular width of one magnet segment
    T = 2*pi/p;             % period of array
    n_array = 1:num_harmonics;
    M_r_n_cos = zeros(1,num_harmonics);
    M_phi_n_sin = zeros(1,num_harmonics);
    for k = 0:N_m
        phi_a_k = max((k-0.5)*del_phi,0);
        phi_b_k = min((k+0.5)*del_phi,T/2);
        if inner_rotor
            phi_k = k*del_phi - k*pi/N_m;
        else
            phi_k = k*del_phi + k*pi/N_m;
        end
```

```
        M_r_n_cos = M_r_n_cos + sin((n_array*p+1)*phi_b_k - phi_k).
           /(2*(n_array*p+1)) + sin((n_array*p-1)*phi_b_k + phi_k).
           /(2*(n_array*p-1));
        M_r_n_cos = M_r_n_cos - sin((n_array*p+1)*phi_a_k - phi_k).
           /(2*(n_array*p+1)) - sin((n_array*p-1)*phi_a_k + phi_k).
           /(2*(n_array*p-1));
        M_phi_n_sin = M_phi_n_sin + sin((n_array*p+1)*phi_b_k - phi_k
           )./(2*(n_array*p+1)) - sin((n_array*p-1)*phi_b_k + phi_k).
           /(2*(n_array*p-1));
        M_phi_n_sin = M_phi_n_sin - sin((n_array*p+1)*phi_a_k - phi_k
           )./(2*(n_array*p+1)) + sin((n_array*p-1)*phi_a_k + phi_k).
           /(2*(n_array*p-1));
    end
    M_r_n_cos = M_r_n_cos * M_o*2*p/pi;
    M_phi_n_sin = M_phi_n_sin * M_o*2*p/pi;
end
```

Function for calculating the harmonics of the rotor field using equation (2.22):

```
function [H_r_n, H_phi_n] = get_H_coefficients(inner_rotor, p, R1, R2
   , R3, R4, a_n, b_n, R_meas)
    n_array = 1:length(a_n);
    if inner_rotor
        x = 0.5*n_array*p./(1-(R1/R4).^(2*n_array*p)).*((a_n+b_n).
           /(1-n_array*p).*((R1/R3).^(2*n_array*p).*(R3/R_meas).^(
           n_array*p+1)-(R1/R2).^(2*n_array*p).*(R2/R_meas).^(n_array
           *p+1)) + ...
            (a_n - b_n)./(1+n_array*p).*((R3/R_meas).^(n_array*p+1)-(
               R2/R_meas).^(n_array*p+1)));
        H_r_n = x.*(1+(R_meas/R4).^(2*n_array*p));
```

```
        H_phi_n = x.*(1-(R_meas/R4).^(2*n_array*p));
    else
        x = 0.5*n_array*p./(1-(R1/R4).^(2*n_array*p)).*((a_n+b_n).
           /(1-n_array*p).*((R_meas/R2).^(n_array*p-1)-(R_meas/R3).^(
           n_array*p-1)) + (-a_n+b_n)./(1+n_array*p).* ...
            ((R3/R4).^(2*n_array*p).*(R_meas/R3).^(n_array*p-1)-(R2/
               R4).^(2*n_array*p).*(R_meas/R2).^(n_array*p-1)));
        H_r_n = -x.*(1+(R1/R_meas).^(2*n_array*p));
        H_phi_n = x.*(1-(R1/R_meas).^(2*n_array*p));
    end
end
```

Function for plotting the rotor field using the harmonic coefficients calculated previously:

```
function [x, y] = get_plot_from_fourier_coefs(odd, coefs, p,
   num_points)
    T = 2*pi/p;
    x = 0:T/num_points:T;
    y = zeros(1,num_points+1);
    for i = 1:length(coefs)
        if odd
            y = y + coefs(i) * sin(i*p*x);
        else
            y = y + coefs(i) * cos(i*p*x);
        end
    end
end
```

Function for calculating the torque produced by a machine with a Halbach array rotor and slotted stator with a concentrated, three-phase winding using equation (2.49):

```
function [time, torque] = get_torque(H_R_n, R, w_e, I_peak, w_so, p,
```

```
   Length)
    u_o = 4*pi*10^-7;
    num_harmonics = length(H_R_n);
    n_array = 1:num_harmonics;
    phi_a = w_so / (2*R);
    T = 2*pi/w_e;
    num_points = 400;
    time = 0:T/num_points:T;
    torque = zeros(1,num_points+1);
    k_n = -4*I_peak*sin(n_array*p*phi_a)./(n_array*pi*w_so);
    for n  = 1:num_harmonics
        if mod(n-1,6) == 0
            % Forward rotating
            torque = torque + H_R_n(n)*k_n(n)*cos(w_e*time*(n-1));
        elseif mod(n+1,6) == 0
            % Backward rotating
            torque = torque + H_R_n(n)*k_n(n)*cos(w_e*time*(n+1));
        end
    end
    torque = -torque * 3/2 * u_o * Length * R^2 * pi;
end
```

References

[1] R. Jansen, C. Bowman, A. Jankovsky, R. Dyson, and J. Felder, "Overview of nasa electrified aircraft propulsion research for large subsonic transports," in *53rd AIAA/SAE/ASEE Joint Propulsion Conference, AIAA Propulsion and Energy Forum*, 2017, pp. 8–27. [Online]. Available: https://ntrs.nasa.gov/archive/nasa/casi.ntrs.nasa.gov/20170012222.pdf.

[2] Z. S. Spakovszky, Y. Chen, E. M. Greitzer, *et al.*, *A megawatt-class electrical machine technology demonstrator for turbo-electric propulsion*, AIAA/IEEE Electric Aircraft Technologies Symposium (EATS), https://hdl.handle.net/1721.1/150870, 2023.

[3] J. Welstead, J. Felder, M. Guynn, B. Haller, M. Tong, S. Jones, I. Ordaz, J. Quinlan, and B. Mason, "Overview of the nasa starc-abl (rev. b) advanced concept," in *One Boeing NASA Electric Aircraft Workshop*, 2017. [Online]. Available: https://ntrs.nasa.gov/api/citations/20170005612/downloads/20170005612.pdf.

[4] A. Dowdle, "Design of a high specific power electric machine for turboelectric propulsion," Ph.D. dissertation, Massachusetts Institute of Technology, 2022.

[5] Y. Chen, "Technology demonstration of a megawatt-class integrated motor drive for aircraft propulsion," Ph.D. dissertation, Massachusetts Institute of Technology, 2023.

[6] M. Qasim, "Design of high speed, high specific power motor drives for megawatt aircraft applications," Ph.D. dissertation, Massachusetts Institute of Technology, 2024.

[7] D. Lee, T. Balachandran, S. Sirimanna, *et al.*, "Detailed design and prototyping of a high power density slotless pmsm," *IEEE Transactions on Industry Applications*, vol. 59, no. 2, pp. 1719–1727, 2023. DOI: 10.1109/TIA.2022.3230379.

[8] J. Swanke, H. Zeng, D. Bobba, T. M. Jahns, and B. Sarlioglu, "Design and testing of a modular high-speed permanent-magnet machine for aerospace propulsion," in *2021 IEEE International Electric Machines and Drives Conference (IEMDC)*, 2021, pp. 1–8. DOI: 10.1109/IEMDC47953.2021.9449536.

[9] Z. Song, C. Liu, K. Feng, H. Zhao, and J. Yu, "Field prediction and validation of a slotless segmented-halbach permanent magnet synchronous machine for more electric aircraft," *IEEE Transactions on Transportation Electrification*, vol. 6, no. 4, pp. 1577–1591, 2020. DOI: 10.1109/TTE.2020.2982733.

[10] Z. Xia, Z. Zhu, and D. Howe, "Analytical magnetic field analysis of halbach magnetized permanent-magnet machines," *IEEE Transactions on Magnetics*, vol. 40, no. 4, pp. 1864–1872, 2004. DOI: 10.1109/TMAG.2004.828933.

[11] *Recoma 35e*, Arnold Magnetic Technologies, 2017. [Online]. Available: https://www.arnoldmagnetics.com/wp-content/uploads/2017/10/Recoma-35E-160205-final.pdf.

[12] Vacuumshmelze, *Soft magnetic cobalt-iron alloys*, https://vacuumschmelze.com/products/soft-magnetic-materials-and-stamped-parts/49-cobalt-iron-vacoflux-and-vacodur, 2021.

[13] A. Moses and B. Thomas, "Stress sensitivity of the a.c. magnetic properties of permendur after various heat treatments," *IEEE Transactions on Magnetics*, vol. 12, no. 2, pp. 103–106, 1976. DOI: 10.1109/TMAG.1976.1059003.

[14] Rembrandtin, *Remisol eb-548 application note*, http://www.polarislaserlaminations.com/548Specs.pdf, 2008.

[15] N. Alatawneh and P. Pillay, "The impact of rotating field on core loss estimation in electrical machine laminations," in *2012 IEEE Energy Conversion Congress and Exposition (ECCE)*, 2012, pp. 2696–2703. DOI: 10.1109/ECCE.2012.6342535.

[16] H. Ebrahimi, Y. Gao, H. Dozono, K. Muramatsu, T. Okitsu, and D. Matsuhashi, "Effects of stress and magnetostriction on loss and vibration characteristics of motor," *IEEE Transactions on Magnetics*, vol. 52, no. 3, pp. 1–4, 2016. DOI: 10.1109/TMAG.2015.2493098.